Semiclassical gravitational collapse of a radially symmetric massless scalar quantum field

Jana N. Guenther,[1,2,*] Christian Hoelbling,[2,†] and Lukas Varnhorst[1,2,‡]

[1]*Aix Marseille Université, Université de Toulon, CNRS, CPT, F-13288 Marseille Cedex 9, France*
[2]*Department of Physics, University of Wuppertal, D-42119 Wuppertal, Germany*

(Received 25 November 2020; accepted 19 April 2022; published 16 May 2022)

We present a method to study the semiclassical gravitational collapse of a radially symmetric scalar quantum field in a coherent initial state. The formalism utilizes a Fock space basis in the initial metric, is unitary and time reversal invariant up to numerical precision. It maintains exact compatibility of the metric with the expectation values of the energy momentum tensor in the scalar field coherent state throughout the entire time evolution. We find a simple criterion for the smallness of discretization effects, which is violated when a horizon forms. As a first example, we study the collapse of a specific state in the angular momentum $l = 0$ approximation. Outside the simulated volume, it produces a Schwarzschild metric with $r_s \sim 3.5\ell_p$. We see behavior that is compatible with the onset of horizon formation both in the semiclassical and corresponding classical cases in a regime where we see no evidence for large discretization artifacts. In our example setting, we see that quantum effects accelerate the possible horizon formation and move it radially outward. We find that this effect is robust against variations of the radial resolution, the time step, the volume, the initial position and shape of the inmoving state, the vacuum subtraction, the discretization of the time evolution operator, and the integration scheme of the metric. We briefly discuss potential improvements of the method and the possibility of applying it to black hole evaporation. We also briefly touch on the extension of our formalism to higher angular momenta but leave the details and numerics for a forthcoming publication.

DOI: 10.1103/PhysRevD.105.105010

I. INTRODUCTION

Ever since Hawking's seminal paper [1], semiclassical effects in the vicinity of horizons have been widely debated in the literature [2–6] (for reviews, see, e.g., [7,8]). A lot of this discussion has focused on the vacuum behavior of quantum fields on a background metric that is supposed to have formed by a different mechanism than by the collapse of the quantum fields themselves. In the classical theory, the formation of a horizon from collapsing scalar fields has been intensively studied numerically [9–20], while for the semiclassical case, we are aware of only one other suggestion for a numerical treatment [21,22], although various other methods have been applied to this problem [23–27].

In this paper, we present a formalism to numerically study the gravitational collapse of a radially symmetric complex scalar quantum field in real time in the angular momentum $l = 0$ approximation.

The fact that the scalar field only interacts semiclassically via gravity allows us to trace its evolution without any Fock space truncation if we remain in the Fock space of the original metric. While it would be extremely complicated to represent the scalar field in the Fock space of the final metric and thus observe the outgoing particle content, we can nonetheless trace the expectation values of crucial quantities such as the Hamiltonian density of the scalar field throughout the entire time evolution and thereby obtain a quantitative picture of the collapse.

One of the main features of our formalism is the guaranteed compatibility of the scalar field with the background metric at all times. Although we can disentangle classical from vacuum contributions and thus explicitly study backreaction effects, the metric is at every point in our time evolution compatible with the corresponding expectation value of the energy-momentum tensor of the scalar field.

Using this new formalism, we then investigate the collapse of one specific field configuration that asymptotically gives a Schwarzschild metric outside of the simulated volume with (in Planck units) $r_s \sim 3.5$. We demonstrate that with very moderate computational effort, our formalism can trace the time evolution of such a state faithfully until about a maximum $r_s/r \sim 0.9$, signifying the onset of horizon formation. We investigate the sizes of discretization and finite volume effects and apply different vacuum

*jguenther@uni-wuppertal.de
†hch@uni-wuppertal.de
‡varnhorst@uni-wuppertal.de

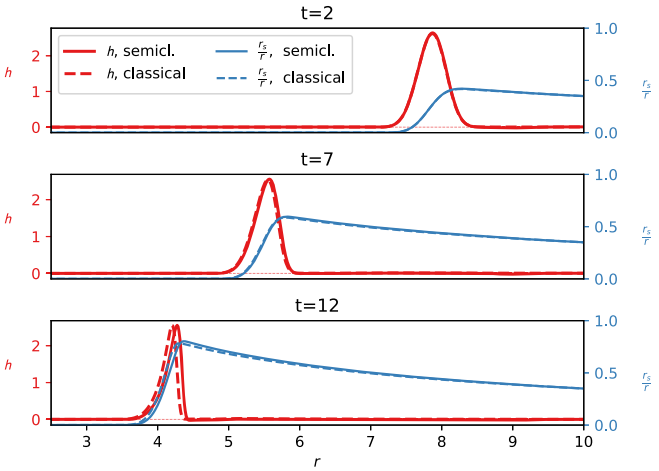

FIG. 1. Three snapshots of the gravitational collapse of a spherically symmetric scalar field. The plots show, for three different asymptotic observer times, the radial Hamiltonian density of the scalar field (or its expectation value in the case of the quantum field) and the ratio of local Schwarzschild radius to radius r_s/r for both the classical and semiclassical case. It is clearly visible that quantum effects increase the peak of the forming horizon as well as shift its location radially outward.

subtraction procedures, discretizations, and integration schemes. In addition, we give a simple criterion that signifies the presence of large discretization artifacts. In our example setting, the onset of the horizon formation in the semiclassical theory happens at larger radii and with a higher r_s/r than in the classical case (see Fig. 1). This finding is corroborated by an energy influx into the region of the forming horizon both from the outside and from the inside.

Continuing our simulations at times even closer to the expected horizont formation, we see a host of new effects that we deem likely to be discretization artifacts.

Although it is well-known that $l = 0$ modes dominate the Hawking radiation in the spherically symmetric case [28], and that the $l = 0$ approximation, which we employ here, can be used to obtain some qualitative insight [29], we would like to stress that it is still an uncontrolled approximation in principle and that taking higher momentum modes into account will be essential for a quantitative understanding. The formalism as presented in this paper is not directly suited for the complete numerical treatment of the system, including the vacuum contributions to the higher angular momentum modes of the scalar field. A generalization taking these modes into account is possible [30] and will be studied in detail in a forthcoming publication.

The paper is structured as follows. In Sec. II, we derive the semiclassical (and classical) equations of motion for coherent states in our original Fock space basis. In Sec. III, we discretize these equations of motion and provide a method for implementing sensible consistent initial states. In Sec. IV, we present the main physics results, and we conclude in Sec. V.

II. DERIVATION OF THE FORMALISM

A. The classical equations of motions

We work in Planck units $\hbar = c = G = 1$. We investigate a radially symmetric classical N_c component complex scalar field $\bar{\phi}$ on a background metric of the form [9],

$$g_{\mu\nu} = \mathrm{diag}(\alpha^2(t,r), -a^2(t,r), -r^2, -r^2\sin^2\theta). \quad (1)$$

From the action,

$$S = \int \mathrm{d}^4x\sqrt{-g}\left(-\frac{1}{16\pi}R + \frac{1}{2}g^{\mu\nu}\bar{\phi}^\dagger_{,\mu}\bar{\phi}_{,\mu}\right),$$

we obtain a complete set of classical equations of motion [9,20]. For the metric part, we have

$$\begin{aligned}\frac{\alpha_{,r}}{\alpha} - \frac{a_{,r}}{a} - \frac{a^2-1}{r} &= 0\\ \frac{a_{,r}}{a} + \frac{a^2-1}{2r} &= \frac{a}{r\alpha}\mathcal{H}_r\\ \frac{a_{,t}}{a} &= \frac{\alpha}{ra}\mathcal{P}_r,\end{aligned} \quad (2)$$

while the evolution of the scalar field is governed by the Hamiltonian $\mathcal{H} = \int_0^\infty \mathrm{d}r\mathcal{H}_r$ arising from the Hamiltonian density,

$$\mathcal{H}_r = \frac{\alpha}{a}\left(\frac{1}{2\pi r^2}\bar{\Pi}\bar{\Pi}^\dagger + 2\pi r^2\bar{\phi}^\dagger_{,r}\bar{\phi}_{,r}\right),$$

where the conjugate momenta are defined as

$$\bar{\Pi} = 2\pi r^2\frac{a}{\alpha}\bar{\phi}^\dagger_{,t} \qquad \bar{\Pi}^\dagger = 2\pi r^2\frac{a}{\alpha}\bar{\phi}_{,t},$$

In addition, a pseudo-momentum density,

$$\mathcal{P}_r = (\bar{\Pi}\bar{\phi}_{,r} + \bar{\Pi}^\dagger\bar{\phi}^\dagger_{,r}),$$

occurs in the last equation in (2). This equation, however, is not independent, and we ignore it in our numerical treatment other than for crosschecking purposes.

We now perform the substitution,

$$\phi = \sqrt{2\pi}r\sqrt{\frac{a^0}{\alpha^0}}\bar{\phi},$$

so that the Hamiltonian density may be written as

$$\mathcal{H}_r = (Q\psi)^\dagger_r(Q\psi)_r, \quad (3)$$

where

$$Q = \begin{pmatrix} q & 0 \\ 0 & A \end{pmatrix} \psi = \begin{pmatrix} \phi \\ \Pi^\dagger \end{pmatrix}, \tag{4}$$

with the diagonal matrix A that has elements,

$$A_r = \frac{a_r^0 \alpha_r}{\alpha_r^0 a_r}. \tag{5}$$

The metric parameters a^0 and α^0 here refer to the values of a and α at a reference time t_0, and the operator q is defined as

$$q = \sqrt{\frac{\alpha}{a}} r \partial_r \sqrt{\frac{\alpha^0}{a^0}} \frac{1}{r}. \tag{6}$$

To facilitate a mode decomposition of the field ϕ, we introduce the singular value decomposition (SVD) of q_0, the operator q at time t_0, as

$$q^0 = U \omega V^T, \qquad \omega = \mathrm{diag}(\omega_1, \omega_2, \ldots). \tag{7}$$

This decomposition allows us to define field modes $\hat{\psi}_k$, which depend on the metric at the reference time t_0, as

$$\psi_r = \int_0^\infty \mathrm{d}k U^*_{rk} \hat{\psi}_k. \tag{8}$$

Here and in the following, quantities with an index k are understood to be related to the modes defined in the above equation. We adopted an index notation for k and r even for the continuous case. Using the basis,

$$\hat{\phi}_k = \frac{(b_-)_k + (b_+)_k^\dagger}{\sqrt{2\omega}} \qquad \hat{\phi}_k^\dagger = \frac{(b_-)_k^\dagger + (b_+)_k}{\sqrt{2\omega}}$$
$$\hat{\Pi}_k = -\frac{(b_-)_k - (b_+)_k^\dagger}{\sqrt{2\omega}} \qquad \hat{\Pi}_k^\dagger = \frac{(b_-)_k^\dagger - (b_+)_k}{\sqrt{2\omega}},$$

we express the Hamiltonian density as

$$\begin{aligned} \mathcal{H}_r = & \frac{1}{2} \int_0^\infty \mathrm{d}k' \int_0^\infty \mathrm{d}k \sqrt{\omega_k \omega_{k'}} A_r \\ & \times (((b_+)_{k'} (b_+)_k^\dagger + (b_-)_{k'}^\dagger (b_-)_k)(U_{rk'} U_{rk} + V_{rk'} V_{rk}) \\ & + ((b_+)_{k'} (b_-)_k + (b_-)_{k'}^\dagger (b_+)_k^\dagger) \\ & \times (U_{rk'} U_{rk} - V_{rk'} V_{rk})). \end{aligned}$$

The poisson brackets of the $(b_\pm)_k$ and $(b_\pm)_k^\dagger$ are

$$\{(b_+)_k, (b_+)_{k'}^\dagger\} = \{(b_-)_k, (b_-)_{k'}^\dagger\} = -i\delta(k - k') \mathbb{1}_f, \tag{9}$$

where $\mathbb{1}_f$ is the unit matrix in component space, and all other Poisson brackets vanish. In the semiclassical theory, the $(b_\pm)_k^\dagger$ and $(b_\pm)_k$ will therefore play the role of creation and annihilation operators of the scalar field.

B. Time evolution of observables

In anticipation of the semiclassical time evolution, we will now develop the equations of motion for the $(b_\pm)_k^\dagger$ and $(b_\pm)_k$, keeping in mind that they can be either complex numbers obeying the canonical equations of motion or operators with commutation relations,

$$[(b_+)_k, (b_+)_{k'}^\dagger] = [(b_-)_k, (b_-)_{k'}^\dagger] = \delta(k - k') \mathbb{1}_f. \tag{10}$$

We start by writing the Hamiltonian in the compact form,

$$\mathcal{H} = b_+ W b_+^\dagger + b_-^\dagger W b_- + b_+ X b_- + b_-^\dagger X b_+^\dagger,$$

where we have defined

$$W_{k'k} = \int_0^\infty \mathrm{d}r \frac{1}{2} \sqrt{\omega_{k'}} \left(U_{rk'} \frac{a_0 \alpha}{\alpha_0 a} U_{rk} + V_{rk'} \frac{a_0 \alpha}{\alpha_0 a} V_{rk} \right) \sqrt{\omega_k}$$

and

$$X_{k'k} = \int_0^\infty \mathrm{d}r \frac{1}{2} \sqrt{\omega_{k'}} \left(U_{rk'} \frac{a_0 \alpha}{\alpha_0 a} U_{rk} - V_{rk'} \frac{a_0 \alpha}{\alpha_0 a} V_{rk} \right) \sqrt{\omega_k}.$$

The Heisenberg equations of the $(b_\pm)_k$ and $(b_\pm)_k^\dagger$ on a given metric then become[1]

$$\begin{aligned} (b_+)_{k,t} &= -i(b_+)_{k'} W_{k'k} - i(b_-)_{k'}^\dagger X_{k'k} \\ (b_-)_{k,t} &= -iW_{kk'}(b_-)_{k'} - iX_{kk'}(b_+)_{k'}^\dagger, \end{aligned} \tag{11}$$

which can easily be shown to be a Bogolyubov [31] transformation in the semiclassical case. We would now like to construct the creation and annihilation operators at a given time $b_\pm^\dagger(t)$ and $b_\pm(t)$ in terms of the same operators $b_\pm^\dagger = b_\pm^\dagger(t_0)$ and $b_\pm = b_\pm(t_0)$ at the reference time t_0. Because of the form of the time evolution (11), we can generically write

$$\begin{aligned} b_+(t) &= b_+ w_+(t) + b_-^\dagger x_+^\dagger(t) \\ b_-(t) &= w_-(t) b_- + x_-^\dagger(t) b_+^\dagger, \end{aligned}$$

with coefficient matrices $w_\pm(t)$ and $x_\pm(t)$ that obviously fulfill the initial conditions,

$$w_\pm(t_0) = \mathbb{1} \qquad x_\pm(t_0) = 0.$$

[1]Here, we introduce an integral convention $x_k y_k := \int_0^\infty \mathrm{d}k x_k y_k$ over continuous momentum modes. For discrete indices, the standard summation convention still applies.

Using these initial conditions and the time evolution of the creation and annihilation operators (11), we find the time evolution of the coefficient matrices to be[2]

$$\dot{w}(t) = -iw(t)W - ix^*(t)X$$
$$\dot{x}(t) = -ix(t)W - iw^*(t)X,$$

where we can identify

$$w(t) = w_+(t) = w_-^T(t) \qquad x(t) = x_+^\dagger(t) = x_-^*(t).$$

Since the time evolution is a Bogolyubov transformation, the coefficient matrices fulfill the identities,

$$\mathbb{1} = w^\dagger(t)w(t) - x^\dagger(t)x(t) \qquad x^T(t)w(t) = w^T(t)x(t).$$

We now define linear combinations,

$$u(t) = (w(t) + x^*(t))\sqrt{\omega}U^T$$
$$v(t) = (w(t) - x^*(t))\sqrt{\omega}V^T,$$

of the coefficient matrices for which the time evolution equations,

$$\dot{u} = -ivAq^{0T}$$
$$\dot{v} = -iuAq^0, \tag{12}$$

are particularly well-suited for a numerical treatment. We can express $\mathcal{H}_r$ and $\mathcal{P}_r$ at an arbitrary time t in terms of these new coefficient matrices and the creation and annihilation operators at the initial time t_0 as

$$\mathcal{H}_r = \frac{1}{2}(b_+v + b_-^\dagger v^*)A_r(v^\dagger b_+^\dagger + v^T b_-) + \frac{1}{2}(b_+u - b_-^\dagger u^*)A_r(u^\dagger b_+^\dagger - u^T b_-) \tag{13}$$

and

$$\mathcal{P}_r = \frac{i}{2}(b_+u + b_-^\dagger u^*)\frac{a_r^0}{\alpha_r^0}(v^\dagger b_+^\dagger - v^T b_-) - \frac{i}{2}(b_+v - b_-^\dagger v^*)\frac{a_r^0}{\alpha_r^0}(u^\dagger b_+^\dagger + u^T b_-). \tag{14}$$

The first two equations of (2) together with (5), (6), (12), (13), (14) and the initial conditions,

$$u(t_0) = \sqrt{\omega}U^T$$
$$v(t_0) = \sqrt{\omega}V^T. \tag{15}$$

[2]We use the shorthand notation $\dot{x} \coloneqq x_{,t}$.

thus form a complete set of equations of motion for the classical case. As a last step, we replace the parameters α and a, describing the metric by the more suitable

$$d = \frac{r}{a^2} \qquad \hat{\alpha} = \alpha a,$$

which we can use to rewrite the equations of motion (2) as

$$\frac{1 - d_{,r}}{d} = \frac{\hat{\alpha}_{,r}}{\hat{\alpha}}$$
$$\frac{1 - d_{,r}}{2d} = \hat{\mathcal{H}}_r$$
$$-\frac{1}{2\hat{\alpha}}\frac{d_{,t}}{d} = \hat{\mathcal{P}}_r, \tag{16}$$

with

$$\hat{\mathcal{H}}_r = \frac{1}{2}(b_+v + b_-^\dagger v^*)\frac{1}{\hat{\alpha}_r^0 d_r^0}(v^\dagger b_+^\dagger + v^T b_-) + \frac{1}{2}(b_+u - b_-^\dagger u^*)\frac{1}{\hat{\alpha}_r^0 d_r^0}(u^\dagger b_+^\dagger - u^T b_-) \tag{17}$$

and

$$\hat{\mathcal{P}}_r = \frac{i}{2}(b_+u + b_-^\dagger u^*)\frac{1}{\hat{\alpha}_r^0 d_r^0}(v^\dagger b_+^\dagger - v^T b_-) - \frac{i}{2}(b_+v - b_-^\dagger v^*)\frac{1}{\hat{\alpha}_r^0 d_r^0}(u^\dagger b_+^\dagger + u^T b_-). \tag{18}$$

The relation to the original densities is given by

$$\hat{\mathcal{H}}_r = \frac{1}{\hat{\alpha}_r d_r}\mathcal{H}_r \qquad \hat{\mathcal{P}}_r = \frac{1}{\hat{\alpha}_r d_r}\mathcal{P}_r. \tag{19}$$

We also recast the auxiliary variable (5) as

$$A_r = \frac{\hat{\alpha}_r d_r}{\hat{\alpha}_r^0 d_r^0},$$

and the operator $q^0 = q(t_0)$ (6)

$$q^0 = \sqrt{r\hat{\alpha}^0 d^0}\,\partial_r\sqrt{\frac{\hat{\alpha}^0 d^0}{r^3}}. \tag{20}$$

Note that $\hat{\mathcal{H}}_r$ does not depend on the current metric at all, but only on the metric at the reference time t_0. It is thus easy to radially integrate the first two equations in (16).

C. Vacuum subtraction and normal ordering

We now proceed to quantize the scalar field in the Heisenberg picture. For this purpose, we can utilize the standard Fock space representation at the reference time t_0, since all the subsequent time evolution is absorbed by the coefficient matrices u and v. We also need to replace the $\mathcal{H}_r$

and $\mathcal{P}_r$ in (2) by expectation values of suitably normal ordered operators.

Let us start by considering a general bilinear operator,

$$O = o^0 + b_+ o^{++} b_+^\dagger + b_-^\dagger o^{--} b_- + b_+ o^{+-} b_- + b_-^\dagger o^{-+} b_+^\dagger.$$

Its vacuum expectation value is

$$\langle 0|O|0\rangle = o^0 + \mathrm{Tr}(o^{++}),$$

and thus, if we want it to vanish, we have to impose the normal ordering condition,

$$o^0 = -\mathrm{Tr}(o^{++}).$$

If we add to the modified Hamiltonian density (17) a constant term $\hat{h}_r^0$ so that

$$:\hat{\mathcal{H}}_r := \hat{h}_r^0 + \hat{\mathcal{H}}_r,$$

the normal ordering condition becomes

$$\hat{h}_r^0 = -\frac{N_c}{2}\frac{1}{\hat{\alpha}_r^0 d_r^0}(v_{kr}^* v_{kr} + u_{kr}^* u_{kr}).$$

Naturally, this condition cannot be satisfied for all times simultaneously. Given the physical situation we are interested in, however, we choose the following two subtraction schemes. First, we simply demand that at our reference time t_0, where the nonzero energy density is far away from a potentially forming horizon, the vacuum expectation value of the Hamiltonian density vanishes. This results in

$$\hat{h}_r^0 = -\frac{N_c}{2}\frac{1}{\hat{\alpha}_r^0 d_r^0}(v_{kr}^*(t_0) v_{kr}(t_0) + u_{kr}^*(t_0) u_{kr}(t_0)), \quad (21)$$

where the initial $u_{kr}(t_0)$ and $v(t_0)$ are given by (15). This fails to exactly reproduce the desired property, namely that the vacuum expectation value of the Hamiltonian density vanishes on a flat background metric, but it approaches it asymptotically as we shift the initial position of our inmoving field farther outward. The second possibility is to try to directly render the Hamiltonian density zero on a flat background metric. To accomplish this, we can in principle define

$$\hat{h}_r^0 = -\frac{N_c}{2}(v_{kr}^{\mathrm{free}*} v_{kr}^{\mathrm{free}} + u_{kr}^{\mathrm{free}*} u_{kr}^{\mathrm{free}}), \quad (22)$$

with the free

$$u^{\mathrm{free}} = \sqrt{\omega_{\mathrm{free}}} U_{\mathrm{free}}^T$$
$$v^{\mathrm{free}} = \sqrt{\omega_{\mathrm{free}}} V_{\mathrm{free}}^T,$$

where U_{free}, V_{free}, and ω_{free} are obtained by an SVD of the free operator,

$$U_{\mathrm{free}} \omega_{\mathrm{free}} V_{\mathrm{free}}^T = q_{\mathrm{free}} = r\partial_r \frac{1}{r}.$$

In this paper, we predominantly use the first definition, but we will also explore the possibility of imposing the second condition in our numerical simulations. Several other subtraction schemes are possible, and it would be interesting to study if they lead to different behaviors. We leave this question for future work. We note in passing that $\langle 0|\hat{\mathcal{P}}(t_0)|0\rangle = 0$, and thus, no vacuum subtraction needs to be applied for this operator.

There is a third type of vacuum subtraction that is interesting purely as an observable. We call it the final state vacuum subtraction, and it consists of subtracting the vacuum Hamiltonian density,

$$\hat{h}_r^0 = -\frac{N_c}{2}\frac{1}{\hat{\alpha}_r d_r}(\bar{v}_{kr}^* \bar{v}_{kr} + \bar{u}_{kr}^* \bar{u}_{kr}), \quad (23)$$

where the

$$\bar{u} = \sqrt{\bar{\omega}}\bar{U}^T$$
$$\bar{v} = \sqrt{\bar{\omega}}\bar{V}^T$$

belong to the operator,

$$\bar{q} = \sqrt{r\hat{\alpha}d}\,\partial_r \sqrt{\frac{\hat{\alpha}d}{r^3}}, \quad (24)$$

that has a singular value decomposition (SVD),

$$\bar{q} = \bar{U}\,\bar{\omega}\,\bar{V}^{\mathrm{T}}. \quad (25)$$

It corresponds to subtracting the vacuum Hamiltonian density of the vacuum state corresponding to the metric parameters $\hat{\alpha} = \hat{\alpha}(t)$ and $d = d(t)$ that have evolved at a time t. Since it is extremely difficult to reexpress states other than the vacuum in this new Fock basis, we will not be using it for the time evolution of our system, but it is nonetheless an interesting observable.

D. Coherent states

Let us now construct a single particle state,

$$|f\rangle = (f_+^\dagger b_+^\dagger + b_-^\dagger f_-)|0\rangle,$$

where the $f_{\pm ik}$ are as of now arbitrary coefficients of the i^{th} field component corresponding to the SVD component (frequency) ω_k. We will use the shorthand notation,

$$b^\dagger = (f_+^\dagger b_+^\dagger + b_-^\dagger f_-),$$

and for convenience, impose unit normalization on the state,

$$\langle f|f\rangle = f_+^\dagger f_+ + f_-^\dagger f_- = 1.$$

Taking the expectation value of $:\hat{\mathcal{H}}_r:$ in this state results in

$$\begin{aligned}\langle f|:\hat{\mathcal{H}}_r:|f\rangle = &\frac{N_c}{2}\frac{1}{\hat{\alpha}_r^0 d_r^0}(v_{kr}^* v_{kr} + u_{kr}^* u_{kr}) + \hat{h}_r^0 \\ &+ \frac{1}{2}\left(f_+^T\left(u^*\frac{1}{\hat{\alpha}_r^0 d_r^0}u^T + v^*\frac{1}{\hat{\alpha}_r^0 d_r^0}v^T\right)f_+^*\right) \\ &+ \frac{1}{2}\left(f_-^\dagger\left(u^*\frac{1}{\hat{\alpha}_r^0 d_r^0}u^T + v^*\frac{1}{\hat{\alpha}_r^0 d_r^0}v^T\right)f_-\right),\end{aligned}$$

while

$$\begin{aligned}\langle f|:\hat{\mathcal{P}}_r:|f\rangle = &\frac{N_c}{\hat{\alpha}_r^0 d_r^0}\mathrm{Im}(v_{kr}^* u_{kr}) \\ &+ \frac{i}{2}\left(f_+^T\left(v^*\frac{1}{\hat{\alpha}_r^0 d_r^0}u^T - u^*\frac{1}{\hat{\alpha}_r^0 d_r^0}v^T\right)f_+^*\right) \\ &+ \frac{i}{2}\left(f_-^\dagger\left(v^*\frac{1}{\hat{\alpha}_r^0 d_r^0}u^T - u^*\frac{1}{\hat{\alpha}_r^0 d_r^0}v^T\right)f_-\right).\end{aligned}$$

It is straightforward to generalize these relations for arbitrary n-particle states,

$$|n\rangle = \frac{1}{\sqrt{n!}}b^{\dagger n}|0\rangle.$$

We will, however, concentrate on unit normalized coherent states,

$$|\lambda\rangle = e^{-\frac{|\lambda|^2}{2}}\sum_{n=0}^{\infty}\frac{\lambda^n}{\sqrt{n!}}|n\rangle,$$

with the coherent state parameter λ. The relevant matrix elements of coherent states are given by

$$\begin{aligned}\langle\lambda|b_{k+}^\dagger b_{k'+}|\lambda\rangle &= |\lambda|^2 f_+(k) f_+^*(k') \\ \langle\lambda|b_{k-}^\dagger b_{k'-}|\lambda\rangle &= |\lambda|^2 f_-^*(k) f_-(k') \\ \langle\lambda|b_{k'+} b_{k-}|\lambda\rangle &= \lambda^2 f_-(k) f_+^*(k') \\ \langle\lambda|b_{k'-}^\dagger b_{k+}^\dagger|\lambda\rangle &= \lambda^{*2} f_-^*(k') f_+(k).\end{aligned}$$

If we thus define

$$l_{k+} = \lambda^* f_+(k) l_{k-} = \lambda f_-(k),$$

we can cast the matrix elements $\hat{\mathfrak{h}}_r = \langle\lambda|:\hat{\mathcal{H}}_r:|\lambda\rangle$ and $\hat{\mathfrak{p}}_r = \langle\lambda|\hat{\mathcal{P}}_r|\lambda\rangle$ into the form,

$$\begin{aligned}\hat{\mathfrak{h}}_r = &\frac{N_c}{2\hat{\alpha}_r^0 d_r^0}(v_{kr}^* v_{kr} + u_{kr}^* u_{kr}) + \hat{h}_r^0 \\ &+ \frac{1}{2\hat{\alpha}_r^0 d_r^0}((l_u)_r^\dagger (l_u)_r + (l_v)_r^\dagger (l_v)_r)\end{aligned} \tag{26}$$

$$\begin{aligned}\hat{\mathfrak{p}}_r = &\frac{N_c}{\hat{\alpha}_r^0 d_r^0}\mathrm{Im}(v_{kr}^* u_{kr}) \\ &+ \frac{1}{2\hat{\alpha}_r^0 d_r^0}((l_u)_r^\dagger (l_v)_r + (l_v)_r^\dagger (l_u)_r),\end{aligned} \tag{27}$$

where

$$\begin{aligned}l_u &= -i(u^\dagger l_+ + u^T l_-) \\ l_v &= v^\dagger l_+ - v^T l_-.\end{aligned} \tag{28}$$

Note that the second line on the rhs of both (26) and (27) are equivalent to the right-hand sides of (17) resp. (18) when substituting $(l_+^\dagger, l_-)$ for $b_\pm$ and thus, correspond to the classical component. The first lines on the rhs of (26) and (27) thus represent the quantum effects. Instead of the classical equations of motion (16), we now have the semiclassical equations of motion,

$$\begin{aligned}\frac{1-d_{,r}}{d} &= \frac{\hat{\alpha}'}{\hat{\alpha}} \\ \frac{1-d_{,r}}{2d} &= \hat{\mathfrak{h}}_r \\ -\frac{1}{2\hat{\alpha}}\frac{d_{,t}}{d} &= \hat{\mathfrak{p}}_{\cdot r}\end{aligned} \tag{29}$$

It is straightforward to show that the third equation is redundant also in the semiclassical case with coherent states and that the entire set of equations is self-consistent. We also find that the quantities $\hat{\mathfrak{h}}$ and $\hat{\mathfrak{p}}$ fulfill a modified continuity equation,

$$\frac{1}{a}\left(\frac{a}{\alpha}\mathfrak{h}\right)_{,t} - \frac{1}{\alpha}\left(\frac{\alpha}{a}\mathfrak{p}\right)_{,r} = 0, \tag{30}$$

where, in accordance with (19), we have

$$\mathfrak{h} = \hat{\alpha} d\hat{\mathfrak{h}} \qquad \mathfrak{p} = \hat{\alpha} d\hat{\mathfrak{p}}, \tag{31}$$

so that $\mathfrak{p}$ gives the direction of the scalar field energy flux with the convention that a positive $\mathfrak{p}$ corresponds to an inward pointing flux.

We will from now on, exclusively focus on states that excite only a single field component, e.g., the first one. We can thus drop the field index component, and the only effect of the additional field components is the enhancement by N_c of the vacuum contribution. Following [27], we use this as a tool to enhance vacuum effects in case one needs them to be more prominent.

III. NUMERICAL IMPLEMENTATION

The first two equations of (29) together with (26), (28), (12), (20), the initial conditions (15), and the SVD (7) form a complete set of equations to describe the time evolution of

our field that we now want to discretize. As noted in the preceding section, we can effectively use the same set of equations to describe both the classical and the semiclassical evolution with the only difference that in the classical evolution, we have to omit the first lines on the rhs of (26). Our numerical integration scheme is based on leapfrogging the scalar evolution equations (12) with a radial integration of the metric according to the first two equations of (29) in such a way as to optimally conserve the Bogolyubov-transformation property of the time evolution.

A. The classical radial integration

Let us first concentrate on the classical radial integration of the metric given $\hat{\mathfrak{h}}_r$. We introduce a set of radial coordinates, r_i, $i = 0, \ldots, N_r$, with $\Delta_i = r_i - r_{i-1} > 0$ and the boundary conditions of our metric, $r_0 = d_0$ and $\hat{\alpha}_{N_r} = \hat{\alpha}(r_{N_r}) = 1$. The latter of the two conditions ensures that our metric is Schwarzschild for $r > r_{N_r}$ (with a Schwarzschild radius $r_{N_r} - d_{N_r}$), while the former places a horizon at r_0 if $r_0 > 0$ or ensures that there is no central singularity at $r = 0$ if $r_0 = 0$. In the numerical part of this paper, we will exclusively study the case $r_0 = 0$, although the algorithm presented is perfectly capable of numerically handling the $r_0 > 0$ case as well.

To integrate the metric, we note that the first two equations of (29) give us

$$\ln(\hat{\alpha})' = 2\hat{\mathfrak{h}},$$

which integrates to

$$\hat{\alpha}_{i-1} = \hat{\alpha}_i e^{-2h_i},$$

where we have defined

$$h_i = \int_{r_{i-1}}^{r_i} dr \hat{\mathfrak{h}}(r).$$

Together with the boundary condition $\hat{\alpha}_{N_r} = 1$, we thus find

$$\hat{\alpha}_i = e^{-2\sum_{j=i+1}^{N_r} h_j}. \tag{32}$$

To obtain $d_i = d(r_i)$, we have to integrate the second equations in (29), i.e.,

$$\frac{1 - d'}{2d} = \hat{\mathfrak{h}}_r.$$

To do so, we must assume a specific shape of the density function in between two discretization points, and varying this shape will result in different discretization errors. For the numerical simulations, we choose either of two shapes, both of which are safe in a sense that they do not produce unwanted horizons ($d(r) = 0$) in between discretization points. The first shape we use is a series of δ-shells,

$$\hat{\mathfrak{h}}(r) = \lim_{\varepsilon \to 0} \begin{cases} \frac{h_i}{\varepsilon} & r_i - \varepsilon < r \leq r_i \\ 0 & \text{else} \end{cases},$$

which results in the recursion relation,

$$d_i = (d_{i-1} + \Delta_i) e^{-2h_i}. \tag{33}$$

The second shape is a piecewise constant function,

$$\hat{\mathfrak{h}}(r) = \frac{h_i}{r_i - r_{i-1}} \qquad r_{i-1} < r < r_i,$$

which results in the recursion relation,[3]

$$d_i = e^{-h_i} \left(d_{i-1} e^{-h_i} + \Delta_i \frac{\sinh(h_i)}{h_i} \right). \tag{34}$$

Either of these two relations allows us to compute the d_i from inside out starting with the boundary condition $d_0 = 0$. We can also see that the relative difference between both recursion relations is of the order h_i, and thus, it is important that the condition,

$$h_i \ll 1, \tag{35}$$

is maintained throughout the entire time evolution. This is not trivial, especially near a forming horizon. From (31), we conclude that for a finite $\mathfrak{h}$, $\hat{\mathfrak{h}}$ diverges when $d \to 0$. Since a horizon is characterized by $d = 0$, our formalism will inevitably break down at some point before a horizon appears.

B. Construction of a consistent initial state

Before we start the time evolution of the scalar field, we need to ensure that we have a consistent initial state; i.e., the initial coherent state coefficients $l_{k\pm}$ when inserted into (26) have to produce an $\hat{\mathfrak{h}}$ that generates the correct initial metric parameters $\hat{\alpha}^0$ and d^0. These parameters occur in the operator q^0 (20) whose SVD (7) in turn provides the basis (15) for the mode expansion of the initial state. To construct such a self-consistent initial state, we start by providing

[3]Note that in the numerical implementation, one can use Horner's method to obtain accurate values of d_i for small h_i. Written in Horner form, the Taylor expansion of the critical function is

$$\frac{\sinh(x)}{x} = 1 + \frac{x^2}{2 \cdot 3} \left(1 + \frac{x^2}{4 \cdot 5} \left(1 + \frac{x^2}{6 \cdot 7} (1 + \ldots) \right) \right).$$

For $x < 0.3$, it is sufficient to use this expansion up to the fifth nontrivial term to guarantee double precision accuracy.

initial $h_i \geq 0$ and the ratio $k_i \in [-1, 1]$. We proceed by constructing from them the initial metric parameters according to (32) and either (33) or (34). This allows us to construct the operator q^0 according to (20) and obtain its SVD (7). Of course, we have to discretize the derivative operator ∂_r in q_0, and we do this by taking the simple forward difference operator. Other options and their consequences are explored in Sec. III.

The next step is to determine the classical part of the initial h_i, which we denote by $h_i^c = h_i - h_i^0$, where h_i^0 is the vacuum contribution. When imposing the normal ordering condition (21), the initial vacuum expectation value $\langle 0|:\hat{\mathcal{H}}_r:|0\rangle = 0$, so $h_i^0 = 0$ and thus, $h_i^c = h_i$. For the normal ordering condition (22), we instead have

$$h_i^0 = \frac{N_c}{2}\frac{1}{\hat{\alpha}_i^0 d_i^0}(v_{ki}^*(t_0)v_{ki}(t_0) + u_{ki}^*(t_0)u_{ki}(t_0)) - \frac{N_c}{2}(v_{ki}^{\text{free}*}v_{ki}^{\text{free}} + u_{ki}^{\text{free}*}u_{ki}^{\text{free}}). \tag{36}$$

It turns out that, especially in regions where $h_i = 0$, we can have a vacuum contribution that is slightly larger than the total $h_i^0 > h_i$. This would imply a negative classical contribution $h_i^c < 0$, which, of course, is impossible. To obtain an approximate free vacuum subtraction, we thus have to modify the initial vacuum contribution slightly. Since it turns out that the overall shape of the vacuum contribution h_i^0 is rather similar to h_i itself up to a multiplicative factor, our preferred choice for an approximate free vacuum subtraction is thus provided by

$$h_i^c = (1 - x)h_i,$$

where the constant x is given by the ratio of the vacuum contribution,

$$x = \frac{h_m^0}{h_m},$$

at the position m of the maximum value of h_i.

With the classical contribution h_i^c thus obtained we construct the

$$(l_u)_i = \text{sign}(k_i)\sqrt{h_i^c\left(1 \mp \sqrt{1 - k_i^2}\right)}$$
$$(l_v)_i = \sqrt{h_i^c\left(1 \pm \sqrt{1 - k_i^2}\right)}$$

and, inverting relation (28) for the initial values $u(t_0)$ and $v(t_0)$ (15), we finally obtain the consistent initial state,

$$l_{k\pm} = \frac{1}{\sqrt{\omega_k}}\sum_{i=1}^{p}\frac{\pm(l_v)_i V_{ik} + i(l_u)_i U_{ik}}{2} \tag{37}$$

C. Initializing the scalar field

The physical situation we are interested in is the gravitational collapse of a scalar field. Accordingly, we would like the initial state to be an inmoving shell. To make it inmoving as much as possible, we choose $k_i = 1$, which results in $p_i(t_0) = h_i(t_0)$, where the h_i and p_i are the discretized versions of (26) and (27),

$$\begin{aligned} h_i &= \frac{N_c}{2\hat{\alpha}_i^0 d_i^0}(v_{ki}^* v_{ki} + u_{ki}^* u_{ki}) + \hat{h}_i^0 \\ &\quad + \frac{1}{2\hat{\alpha}_i^0 d_i^0}((l_u)_i^\dagger (l_u)_i + (l_v)_i^\dagger (l_v)_i) \\ p_i &= \frac{N_c}{\hat{\alpha}_i^0 d_i^0}\text{Im}(v_{ki}^* u_{ki}) + \frac{1}{2\hat{\alpha}_i^0 d_i^0}((l_u)_i^\dagger (l_v)_i + (l_v)_i^\dagger (l_u)_i) \\ l_u &= -i(u^\dagger(t)l_+ + u^T(t)l_-) \\ l_v &= v^\dagger(t)l_+ - v^T(t)l_-. \end{aligned} \tag{38}$$

We are still left with the choice of the exact shape of h_i. One could in principle take a thin shell at some radius r_e, i.e., $h_i \propto \delta_{ie}/\Delta_e$, but this or similar choices have a lot of high frequency (i.e., large ω) components that we would like to avoid. We therefore choose to smear out the thin shell to a bump that has a finite support $[R - \sigma, R + \sigma]$. When studying discretization artifacts, we choose the width of the bump to stay constant in physical units. We therefore initialize

$$h_i(t_0) = \begin{cases} \Delta_i f_{\sigma,\lambda}(r_i - R) & |R - r_i| < \sigma \\ 0 & |R - r_i| \geq \sigma. \end{cases} \tag{39}$$

In this paper, we use either one of two window functions. The first one, which we use for our main results, is the Nuttall bump function [32] that has the form,

$$f_{\sigma,\lambda}(x) = \lambda\sum_{k=0}^{3} a_k \cos\left(k\frac{2\pi(x + \sigma)}{\sigma}\right), \tag{40}$$

with the coefficients,

$$\begin{aligned} a_0 &= 0.355768 \\ a_1 &= -0.487396 \\ a_2 &= 0.144232 \\ a_3 &= -0.012604, \end{aligned}$$

and a normalization factor λ that determines the bump height. The second, which we use as a cross-check, is

$$f_{\sigma,\lambda}(x) = \lambda e^{\frac{\sigma^2}{\sigma^2 - x^2}}. \tag{41}$$

We prefer the Nuttall function as it excites high frequency components (in ω_k) less. Since the Nuttall function is

designed to suppress high frequency components in Fourier space as opposed to our U-V basis, further improvement that is targeted to the specific basis should be possible. We do not, however, investigate this in the current paper but leave it for future studies.

D. Time evolution of the scalar field

Our next task is to evolve the scalar field component matrices u and v according to (12) with the initial condition (15). The update should be as close as possible to an exact Bogolyubov transformation. We start out by noting that we can write (12) in the form,

$$\dot{u}\sqrt{\frac{\hat{\alpha}d}{\hat{\alpha}^0 d^0}} = -iv\sqrt{\frac{\hat{\alpha}d}{\hat{\alpha}^0 d^0}}\bar{q}^T$$
$$\dot{v}\sqrt{\frac{\hat{\alpha}d}{\hat{\alpha}^0 d^0}} = -iu\sqrt{\frac{\hat{\alpha}d}{\hat{\alpha}^0 d^0}}\bar{q},$$

with the operator (24) that has an SVD (25). We define

$$g = \sqrt{\frac{\hat{\alpha}d}{\hat{\alpha}^0 d^0}} \qquad H = g\begin{pmatrix} 0 & \bar{U}\,\bar{\omega}\,\bar{V}^{\mathrm{T}} \\ \bar{V}\,\bar{\omega}\,\bar{U}^T & 0 \end{pmatrix} g^{-1},$$

and write the time evolution in matrix form as

$$(\,\mathrm{d}u \quad \mathrm{d}v\,) = -i(\,u \quad v\,)H\mathrm{d}t.$$

Assuming constant metric parameters and thus constant g, we can integrate this expression over a finite time intervall Δt and obtain

$$(\,u(t+\Delta t) \quad v(t+\Delta t)\,) = (\,u(t) \quad v(t)\,)e^{-iH\Delta t}.$$

Computing the matrix exponential, we find

$$e^{-iH\Delta t} = g\begin{pmatrix} \bar{U}\cos(\bar{\omega}\Delta t)\bar{U}^{\mathrm{T}} & -i\bar{U}\sin(\bar{\omega}\Delta t)\bar{V}^{\mathrm{T}} \\ -i\bar{V}\sin(\bar{\omega}\Delta t)\bar{U}^T & \bar{V}\cos(\bar{\omega}\Delta t)\bar{V}^{\mathrm{T}} \end{pmatrix} g^{-1}.$$

A constant metric during the time evolution of the scalar field is of course an approximation that introduces finite time step discretization errors. In order to keep these small, we implemented an update scheme that leapfrogs the time evolution of the scalar field with the radial integration of the metric. In particular, we start out with an implicit time step that updates u and v from $t-\Delta t$ to the time t according to

$$\begin{aligned} u(t) &= u(t-\Delta t)g\bar{U}\cos(\bar{\omega}\Delta t)\bar{U}^{\mathrm{T}}g^{-1} \\ &\quad - iv(t-\Delta t)g\bar{V}\sin(\bar{\omega}\Delta t)\bar{U}^{\mathrm{T}}g^{-1} \\ v(t) &= v(t-\Delta t)g\bar{V}\cos(\bar{\omega}\Delta t)\bar{V}^{\mathrm{T}}g^{-1} \\ &\quad - iu(t-\Delta t)g\bar{U}\sin(\bar{\omega}\Delta t)\bar{V}^{\mathrm{T}}g^{-1}, \end{aligned} \tag{42}$$

where the metric parameters d and $\hat{\alpha}$ that occur in g are those at time t. To obtain these metric parameters, we start by first evaluating (42) with the metric parameters at $t-\Delta t$. We then start an iteration by first computing h_i according to (38). This allows us to compute updated metric parameters d and $\hat{\alpha}$ according to (32) and either (33) or (34) that we can plug in to $\bar{q}$ (24) and g. Following an other SVD (25), we can complete one iteration step by reevaluating (42). This iteration is repeated until the metric parameters converge, which is typically achieved after a few steps for cases of interest. After having successfully iterated the metric parameters d and $\hat{\alpha}$ and thus, g at time t, we complete the update by performing an explicit time step,

$$\begin{aligned} u(t+\Delta t) &= u(t)g\bar{U}\cos(\bar{\omega}\Delta t)\bar{U}^{\mathrm{T}}g^{-1} \\ &\quad - iv(t)g\bar{V}\sin(\bar{\omega}\Delta t)\bar{U}^{\mathrm{T}}g^{-1} \\ v(t+\Delta t) &= v(t)g\bar{V}\cos(\bar{\omega}\Delta t)\bar{V}^{\mathrm{T}}g^{-1} \\ &\quad - iu(t)g\bar{U}\sin(\bar{\omega}\Delta t)\bar{V}^{\mathrm{T}}g^{-1}, \end{aligned}$$

with them. One can show that this update is an exact Bogolyubov transformation, which in the component matrix basis is equivalent to the condition,

$$\mathrm{Re}(u^\dagger(t)v(t)) = q^0,$$

being fulfilled for all times t.

E. Absorbing boundary conditions

The update algorithm detailed thus far is unitary and has, apart from numerical errors, an exact time reversal symmetry. A wave packet that hits the outer boundary r_p of our discretized space will be reflected. Of course, this is a finite volume effect and can in principal be remedied by expanding the range of our discretization. However, if we are willing to give up unitarity, we can implement absorbing boundary conditions, for the classical part at least, by modifying the initial state at every time step. Let us for this purpose define the classical part of h_i and p_i from (38),

$$h_i^c = \frac{1}{2\hat{\alpha}_i^0 d_i^0}((l_u)_i^\dagger(l_u)_i + (l_v)_i^\dagger(l_v)_i)$$
$$p_i^c = \frac{1}{2\hat{\alpha}_i^0 d_i^0}((l_u)_i^\dagger(l_v)_i + (l_v)_i^\dagger(l_u)_i),$$

and impose the condition that both h^c and p^c vanish on the outermost coordinate r_{N_r}, i.e., $h_{N_r}^c = p_{N_r}^c = 0$. This condition implies

$$(l_u)_i = (l_v)_i = 0,$$

which, according to the relation (28), requires a change in the coherent state coefficients $l_\pm$. According to (37), these coefficients have the form,

$$l_\pm = \pm l_R + i l_I \tag{43}$$

with real l_R and l_I, which we want to preserve. We thus plug the ansatz (43) into (28) and solve for l_R and l_I. The result is

$$l_R = \frac{1}{2}(v_R^T + v_I^T u_R^{T-1} u_I^T)^{-1}(l_v - v_I^T u_R^{T-1} l_u)$$
$$l_I = \frac{1}{2}(u_R^T + u_I^T v_R^{T-1} v_I^T)^{-1}(l_u + u_I^T v_R^{T-1} l_v),$$

where $u_{R/I}$ and $v_{R/I}$ are the real resp. imaginary parts of u and v. Obviously, this modification of the state is not part of the time evolution in the Heisenberg picture. We could in principle model the absorbed component as an outgoing classical wave packet in some approximation for $r > r_{N_r}$ and feed the resulting $\hat{\alpha}_{N_r} < 1$ back into the radial integration of the metric as a boundary condition. For the sake of simplicity, however, we restrict ourselves to maintaining $\hat{\alpha}_{N_r} = 1$, which implies that the absorbed component vanishes in a truly unphysical way.

F. Numerical stability

Having implemented the algorithm we described above numerically in double precision arithmetic, we encountered problems with numerical stability of the SVD in certain cases. Specifically, if $r_0 = 0$ and the r_i are evenly spaced, the numerical inaccuracies in the vacuum component of the h_1 increase exponentially once we have $N_r \gtrsim 200$ discretization points. Of course, one can solve this problem by increasing the numerical precision, which is, however, extremely expensive in terms of computer time. Fortunately, there is an alternative for the specific physical situation that we are interested in: Initially, (i.e., at time t_0), we choose the scalar field configuration as a thick shell that has vanishing $\hat{\mathfrak{h}}(r) = \hat{\mathfrak{p}}(r) = 0$ for $r < R_0$. With the specific window functions, we have defined in (39), we have $R_0 = R - \sigma$. We can thus integrate the trajectory $r_{\mathrm{cut}}(t)$ of a lightlike test particle that is radially free falling toward the center starting from R_0 at t_0. If we exclude causality violations (which can only appear as discretization effects), we know that at the time t we should have vanishing $\hat{\mathfrak{h}}(r) = \hat{\mathfrak{p}}(r) = 0$ inside a shell $r < r_{\mathrm{cut}}(t)$. Imposing this condition during the update, i.e., explicitly setting to zero all h_i for which $r_i < r_{\mathrm{cut}}(t)$, will thus remove these particular discretization artifacts.

In order to implement this procedure, we need to integrate the trajectory of our test particle. A radially ingoing lightlike geodesic in our metric is characterized by

$$\mathrm{d}t = -\frac{\hat{\alpha} d}{r}\mathrm{d}r.$$

In a region where $\hat{\mathfrak{h}} = 0$ (which applies to the entire region that our test particle is free falling through), $\hat{\alpha}$ and $\rho = r - d$ are constant, and the geodesic integrates to

$$(t_1 - t_2)\hat{\alpha} = r_2 - r_1 + \rho \ln \frac{r_2 - \rho}{r_1 - \rho}.$$

Solving explicitly for r_2, we obtain

$$r_2 = \rho + W_0((r_1 - \rho)e^{r_1 - \rho + (t_1 - t_2)\hat{\alpha}}),$$

where $W_0(x)$ is the principal branch of the Lambert W-function. When performing a complete update step of our scalar field and the metric by a time interval Δt, we thus need to update the cutoff radius as

$$r_{\mathrm{cut}}(t + \Delta t) = \rho + W_0((r_{\mathrm{cut}}(r) - \rho)e^{r_{\mathrm{cut}}(t) - \rho + \Delta t \hat{\alpha}}).$$

IV. RESULTS

A. Simulation setup

We will now concentrate on one specific physical situation, which is that of an $N_c = 2$ component field that is in a geometry with no preexisting horizon, i.e., $r_0 = 0$. We will also choose a uniform discretization in the radial coordinate r, i.e., $r_i - r_{i-1} = \Delta$, for all $i = 1, \ldots, N_r$. Although nonuniform discretizations would be desirable and are in principle possible with our formalism, we observed partial reflection phenomena at the boundary between different Δ_i whose further investigation we leave open for future studies. We vary the physical size r_{N_r} of our discretized system to be either 10, 12, or 14 and at $t_0 = 0$, place initially inmoving bumps of the generic form (39), with width $\sigma = 1$ at either $R = 9$, 11, or 13, with the obvious restriction $R < r_{N_r}$ so that the bump fits into the discretized system. The size of the initial bump is chosen such that the effective Schwarzschild radius of the outermost shell is $\rho_{N_r} = r_{N_r} - d_{N_r} \cong 3.5$. We have different radial discretizations in steps of factors 2 between $\Delta = 0.1$ and $\Delta = 0.00625$ corresponding, for a system size of $r_{N_r} = 10$, to $N_r = 100$, 200, 400, 800, and 1600 and time steps $\Delta t = 0.001$, 0.002, and 0.004. In the following discussion, we will use as a default case the system with $r_{N_r} = 10$ ($R = 9$), $N_r = 800$, $\Delta t = 0.004$, a Nuttall bump shape (40), a simple forward difference discretization of the derivative operator in (20), (24), an initial state vacuum subtraction (21), and a δ-shell radial integration (33) with reflecting boundary conditions.

Note that on a technical level, the time evolution of the classical field is equivalent to setting $N_c = 0$ in (38). When we refer to the vacuum and classical contributions to any observable, we generically mean the coefficient of the term proportional to N_c and the rest. We can thus refer to the "vacuum contribution" even in the classical ($N_c = 0$) case,

TABLE I. The maximum time for which the criterion (44) is fulfilled for our semiclassical default case and its variations due to different radial discretization.

N_r	t_{safe}
100	4.8
200	8.9
400	12.1
800	14.8
1600	17.5

where it does not contribute toward the time evolution at all. Thus defined, we can directly compare the vacuum contributions of the classical and semiclassical time evolution, which is useful for estimating backreaction effects.

Throughout the time evolution of our system, we will monitor how well the condition (35) is fulfilled, which is necessary for radial discretization effects to be small. For this reason, we will define a safe zone through the criterion,[4]

$$\max_i(h_i) = \max(\Delta\hat{\mathfrak{h}}) < 0.08, \tag{44}$$

which we will elaborate on in Sec. IV C. For our default case, this translates into a safe zone of $t \lesssim 14.8$ with values for other discretizations listed in Table I.

Note that this criterion is a necessary but not a sufficient condition for the smallness of discretization artifacts.

B. Qualitative behavior of the system

Let us first look at the time evolution of our default case in the safe zone. In Fig. 2, we compare at three different (asymptotic coordinate) times t the semiclassical ($N_c = 2$) to the classical ($N_c = 0$) time evolution. We plot the Hamiltonian density[5] $\mathfrak{h} = \hat{\alpha} dh$ together with the metric parameter $r_s/r = 1 - d/r$ that indicates how far away a system is at any given point from forming a horizon. The behavior of both the classical and the semiclassical case is consistent with a forming horizon. We note, however, that quantum effects both enhance the peak in r_s/r and shift it radially outward. This behavior is also evident when looking at the original metric parameters α and a (Fig. 3).

To identify the origin of this quantum effect, we plot in Fig. 4 the vacuum contribution to the Hamiltonian density $\mathfrak{h}^0$ together with the vacuum contribution $\mathfrak{p}^0$ of $\mathfrak{p}$, which is related to $\mathfrak{h}$ by a modified continuity equation (30) and thus, akin to a momentum density. We see that for all three time slices plotted in Fig. 4, $\mathfrak{p}^0$ has the structure of a leading

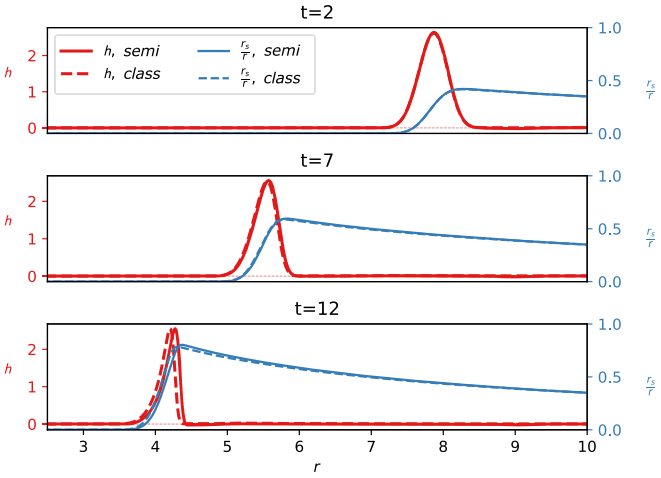

FIG. 2. Time evolution of the Hamiltonian density $\mathfrak{h}$ and the local r_s/r for our default run. We can clearly see the onset of horizon formation. In the semiclassical case, the horizon formation is both more pronounced and happening at larger r.

negative region followed by a trailing positive one. The zero crossing happens close to the point of maximum $\mathfrak{h}$ (see Fig. 5). Remembering that in our convention, a positive value of $\mathfrak{p}$ signifies a radial influx, while a negative value corresponds to an outflux, the shape of $\mathfrak{p}^0$ tells us that quantum effects tend to increase the peak in the Hamiltonian density $\mathfrak{h}$ at the expense of the neighboring regions in this phase of the collapse. This is clearly visible in the shape of $\mathfrak{h}^0$, which has a peak flanked on either side by regions where it is negative. It is also interesting to note that this structure is even visible in the classical case with the peak of $\mathfrak{h}^0$ shifted accordingly, so that it is slightly outward of the peak of $\mathfrak{h}$ as it is in the semiclassical case. In

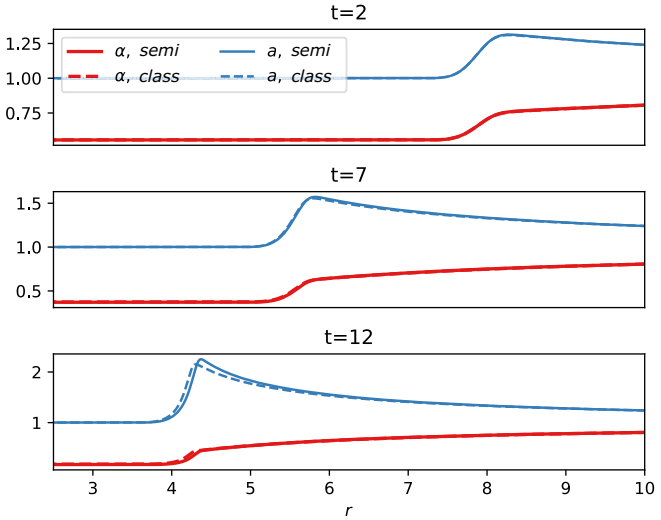

FIG. 3. Time evolution of the metric parameters α and a for our default run. The sharper and more radially outward onset of horizon formation in the semiclassical case is clearly visible.

[4]The specific value 0.08 used in this criterion applies to the Nuttall bump shape and may vary slightly for other shapes.

[5]For simplicity, we will routinely omit to mention that we are looking at expectation values in the semiclassical case and assume that this is implied.

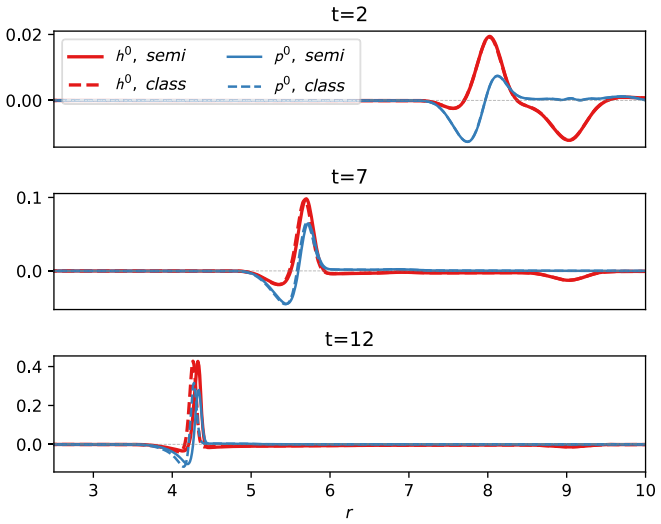

FIG. 4. Time evolution of the vacuum contributions to the densities $\mathfrak{h}$ and $\mathfrak{p}$. For all times shown, the shape of $\mathfrak{p}^0$ consists of a negative bump interior to the forming horizon and a positive bump outside of it, indicating an additional energy influx toward the horizon forming region from both the inside and the outside. Correspondingly, the vacuum contribution to the energy density $\mathfrak{h}^0$ is positive in the horizon forming region and negative just outside it. The dip in $\mathfrak{h}^0$ at the original position of the bump $r = 9$ is an effect of the vacuum subtraction procedure.

Fig. 5, we plot the relevant portion of the $t = 12$ panel of Fig. 4, where these features are clearly distinguishable.

In order to give a visual illustration of the time evolution of our default system, we provide in Fig. 6 a contour plot the Hamiltonian density $\mathfrak{h}$ for the time evolution up to $t = 20$ that compares the classical to the semiclassical evolution.

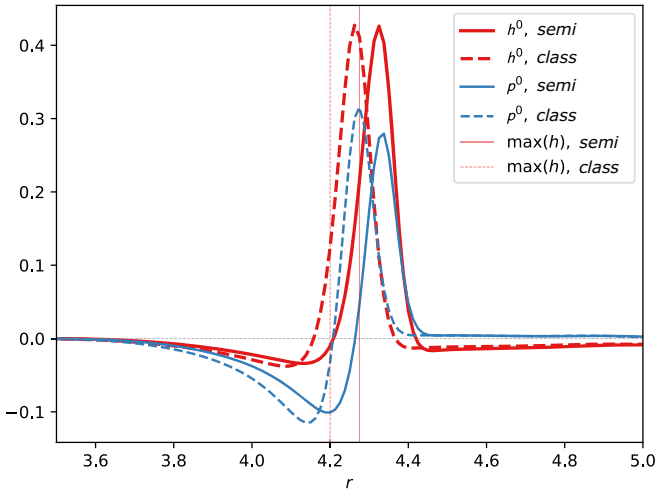

FIG. 5. A more detailed look at the relevant region of the $t = 12$ panel of Fig. 4. Horizontal lines indicate the peak position of the total Hamiltonian density $\mathfrak{h}$. It is evident that quantum effects increase the peak height of $\mathfrak{h}$ and shift it outward while slightly decreasing its value in the immediate vicinity.

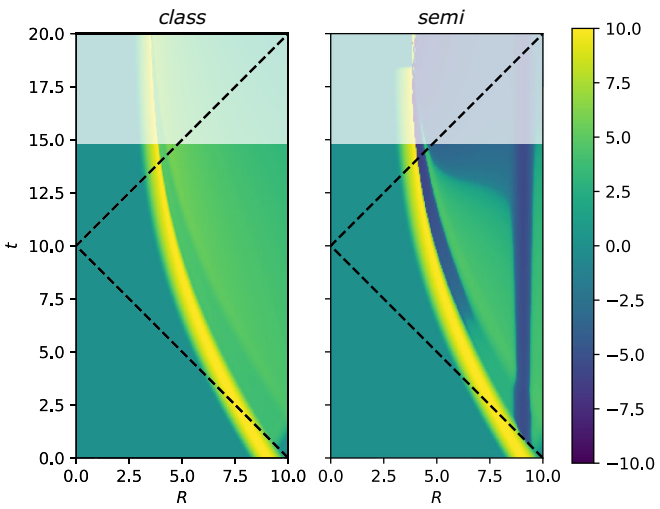

FIG. 6. Contour plot the function $\mathrm{sign}(\mathfrak{h})\ln(1+10^4|\mathfrak{h}|)$ of the Hamiltonian density $\mathfrak{h}$ for the time evolution of our default system. The shaded area on top corresponds to the unsafe zone $t \gtrsim 14.8$. The black dashed diagonal lines correspond to $\mathrm{d}r = \pm\mathrm{d}t$ and indicate the trajectory of a radially infalling massless test particle on a fictitious flat background metric.

The final observable we would like to present is the "final state" vacuum contribution to the Hamiltonian density $\mathfrak{h}^0_f$. We define it as the vacuum contribution to the Hamiltonian density, but with a vacuum subtraction term (23) related to the vacuum that corresponds to the metric parameters $\hat{\alpha} = \hat{\alpha}(t)$ and $d = d(t)$ at the given time t in the evolution. We plot this quantity in Fig. 7 for three different times. As can be seen, according to the final state vacuum, quantum effects lead to a depletion of energy inside the forming horizon and an enhancement outside. In Fig. 8, we compare the vacuum contribution to the Hamiltonian density $\mathfrak{h}^0$ with its final state counterpart $\mathfrak{h}^0_f$.

C. Radial discretization

If we look at the time evolution of the default case beyond the safe zone $t \gtrsim t_{\mathrm{safe}}$, we see the gradual onset of radial discretization artifacts, mainly through high frequency modes. This behavior is displayed in Fig. 9, where we compare the results for our default case to those of the same system but with a radial discretization Δ that is twice as fine, i.e., $N_r = 1600$.

For this finer discretization, the safe zone extends to $t \lesssim 17.5$. We can clearly see that when we are within the safe zone of both systems, the results of both discretizations agree (top panel of Fig. 9). At a time that is out of the safe zone for the coarser discretization but still within the safe zone of the finer one (middle panel), the coarser discretization starts to exhibit high frequency discretization artifacts, while the finer discretization does not. Finally, when we are out of the safe zone of both systems (bottom panel), the finer discretization shows high frequency discretization artifacts as well. We have checked that this

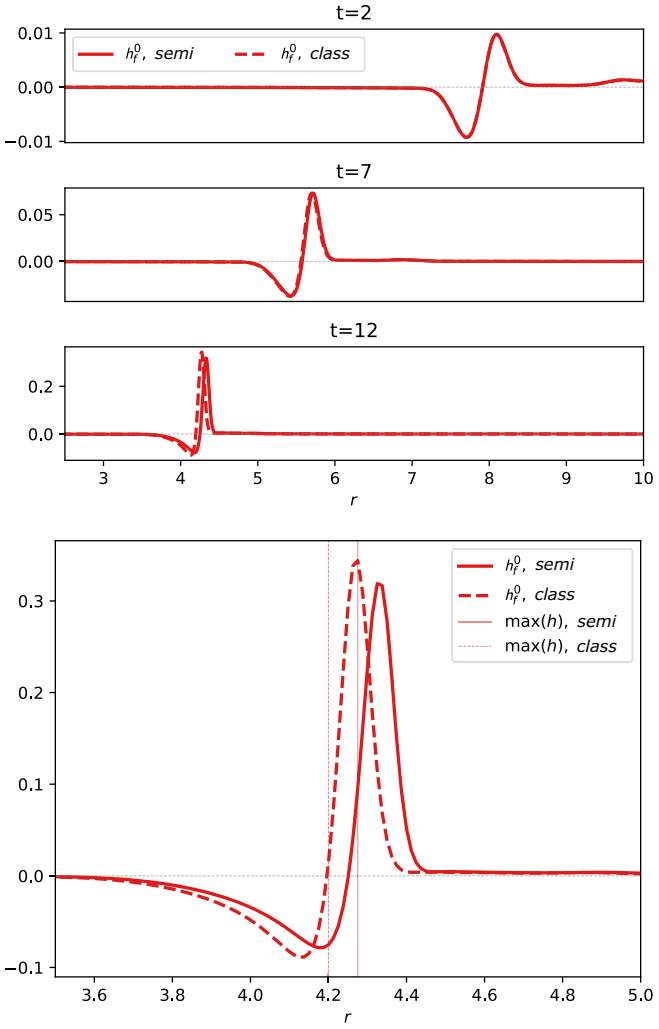

FIG. 7. Time evolution of the final state vacuum contribution to the Hamiltonian density $\mathfrak{h}_f^0$ for three different times (top) and a detail from $t = 12$ (bottom). Horizontal lines indicate the peak position of the total Hamiltonian density $\mathfrak{h}$. From the perspective of the final state vacuum, quantum effects deplete the energy density inside the forming horizon and enhance it outside.

behavior is generically true also for the even coarser discretizations, which is why we believe (44) to be a reasonable criterion for the specific bump shape we use. In Fig. 10, we plot the Hamiltonian density $\mathfrak{h}$, its vacuum contribution $\mathfrak{h}^0$, and r_s/r for all five radial discretizations at the time $t = 12$. At this time, we are, according to Table I, out of the safe zone for our two coarsest discretizations with $N_r = 100$, 200 but within the safe zone of all discretizations with $N_r = 400$ or finer.

Finally, we turn again to our safe zone criterion (44). In Fig. 11, we show the time evolution of $\max_i(h_i)$ for the various discretizations, from which we can read off the extent of the safe zone t_{safe} that we give in Table I.

Interestingly, there is a marked increase of $\max_i(h_i)$ just barely outside the safe zone of our finest discretization. If this would happen in a region where we could trust our

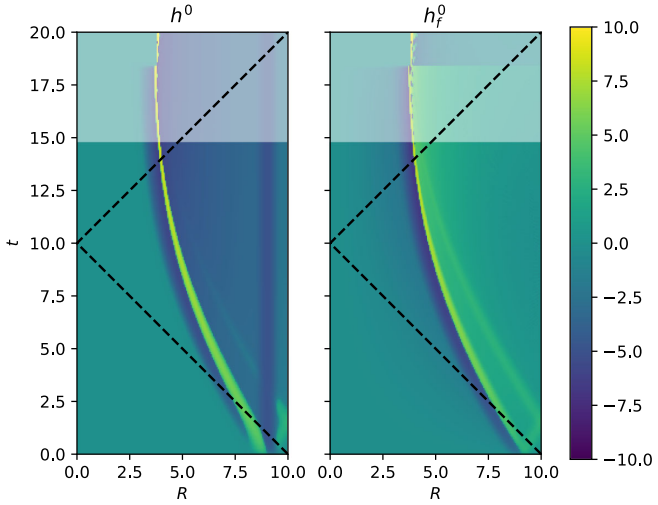

FIG. 8. Comparison of $\mathfrak{h}^0$ with $\mathfrak{h}_f^0$. In each case, we plot the function $\text{sign}(x)\ln(1+10^4|x|)$ where x is either $\mathfrak{h}^0$ or $\mathfrak{h}_f^0$. The shaded area on top corresponds to the unsafe zone $t \gtrsim 14.8$. The black dashed diagonal lines correspond to $\mathrm{d}r = \pm\mathrm{d}t$ and indicate the trajectory of a radially infalling massless test particle on a fictitious flat background metric.

simulation, it would be indicative of a forming horizon. Since it is beyond the safe region, however, we can not exclude that it is purely a discretization artefact. Nonetheless, in the semiclassical simulation, a horizon is actually forming around this time, and we see $d \to 0$ there.

The $\max_i(h_i)$ that we have plotted in Fig. 11 is relevant for algorithmic consideration, but not directly suitable for

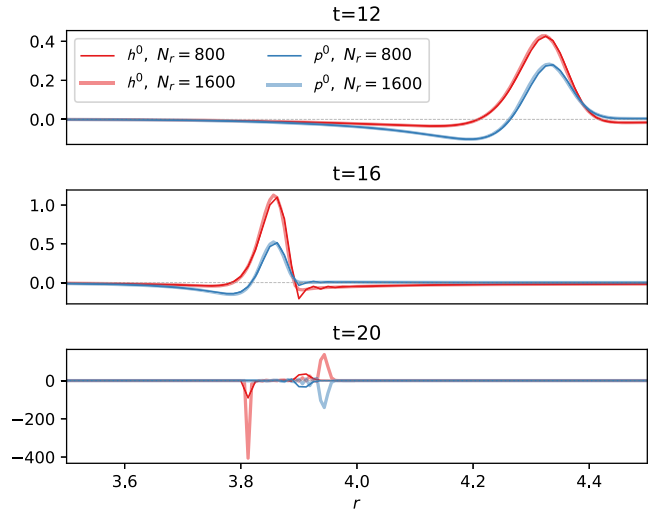

FIG. 9. Comparison between two different radial discretizations $N_r = 800$, 1600 of the same physical system at different times t. The top panel represents a time that is in the safe zone of both discretizations, while the middle panel corresponds to a time that is out of the safe zone of the coarser $N_r = 800$ discretization, while still being inside the safe zone of the finer $N_r = 1600$ case. The bottom panel shows a time that is out of the safe zone even for the finer discretization.

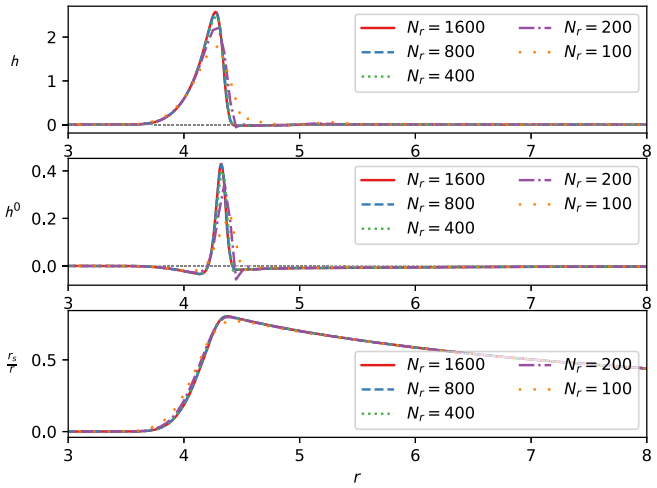

FIG. 10. Comparison of different radial discretizations at $t = 12$. One can see that for $N_r = 100, 200$, this time is outside the safe zone, while it is still inside for the finer discretizations.

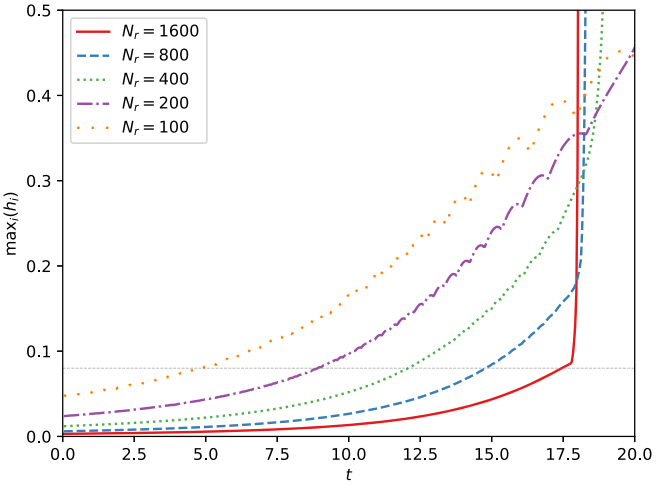

FIG. 11. Comparison of the algorithmically relevant quantity $\max_i(h_i)$ for different radial discretizations. The horizontal line is at 0.08, corresponding to the criterion (44).

physical comparisons as it contains the radial discretization length Δ via $h_i = \hat{\mathfrak{h}}_i \Delta$. We can instead compare $\max_i(\hat{\mathfrak{h}}_i) = \max_i(h_i)/\Delta$ that is a physical density. This comparison is depicted in Fig. 12. We see that initially all curves agree and that the coarser discretizations branch off from the rest of the curves around their respective t_{safe}. Interestingly, it seems that outside of the range of validity, the coarser the discretization, the less likely it is to lead to horizon formation.

D. Discretizing the derivative operator

In the default case, we use the simple forward difference operator,

$$(\nabla_f)_{ij} = \frac{\delta_{i+1,j} - \delta_{i,j}}{\Delta},$$

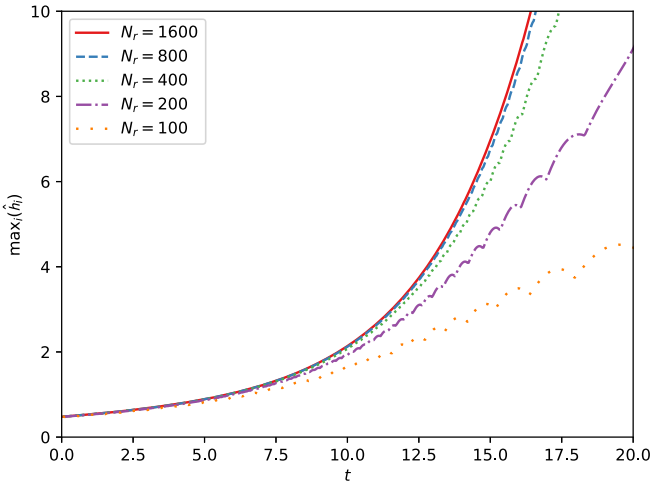

FIG. 12. Comparison of the physically relevant quantity $\max_i(\hat{\mathfrak{h}}_i)$ for different radial discretizations.

to discretize the derivative in (20), (24). To estimate the effect that this choice has on our result, we investigate three other choices. The first two are the backward difference operator $\nabla_b = \nabla_f^T$ and the symmetric difference operator $\nabla = (\nabla_f + \nabla_b)/2$. Both the forward and the backward difference operator have discretization effects that are formally of the order $\partial - \nabla_{f/b} = O(\Delta)$, while for the symmetric difference operator, we have $\partial - \nabla = O(\Delta^2)$. In addition to these two choices, we also investigate a more extended difference operator that involves two points in forward and one in backward direction,

$$(\nabla_x)_{ij} = \frac{1}{\Delta} \sum_{k=-1}^{2} c_k \delta_{i+x,j},$$

where the c_k are fixed such that the discretization effects are $\partial - \nabla_x = O(\Delta^3)$.

In Fig. 13, we compare the Hamiltonian density $\mathfrak{h}$ and its vacuum contribution $\mathfrak{h}^0$ at time $t = 12$ for all discretizations. One can see that despite the differences, the qualitative behavior of all four discretizations is the same. We also note that for the symmetric difference operator, we see a marked increase of high frequency discretization artifacts. This is not surprising, as the symmetric difference operator has problems disentangling low and very high frequency modes.[6] For the remaining three discretizations we show in

[6]We can see a related phenomenon in the simple case of applying the symmetric difference operator to a Fourier mode $f_k(x) = \exp(-ikx)$, which results in $(\nabla f)(x) = i\frac{\sin(\Delta k)}{\Delta} f(x)$. Thus, to the operator ∇, the Fourier modes of momentum k and $\pi/\Delta - k$ are indistinguishable. More concretely, the exclusive even-odd coupling of the operator q^0 enforces opposing checkerboard patterns of the coefficient matrices u and v. Among other things, this forces the diagonal elements of $u^\dagger v$ to vanish, which, in the light of the continuity equation (30), is a particularly unwelcome discretization artifact.

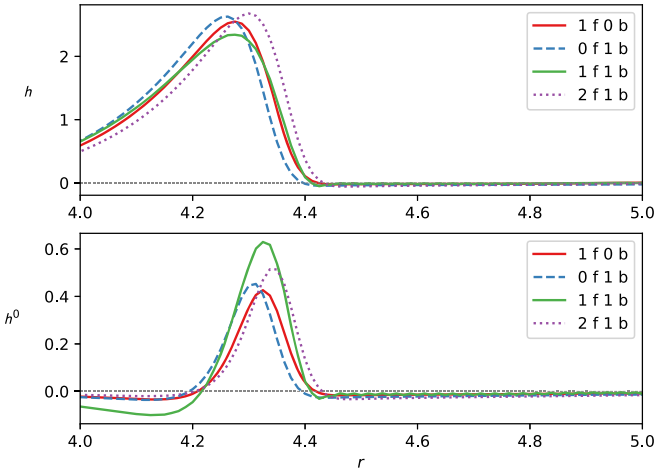

FIG. 13. Hamiltonian density $\mathfrak{h}$ and its vacuum contribution $\mathfrak{h}^0$ at time $t = 12$ for the semiclassical case and various discretizations of the derivative operator. The labels correspond to the number of forward (f) and backward (b) points included in the discretized derivative.

Fig. 14, the difference between the classical and semiclassical $\mathfrak{h}^0$ at $t = 12$. We can clearly see that the feature of a more outward lying semiclassical peak that is enhanced by quantum effects is equally present for all three discretizations of the derivative operator.

The difference between the discretizations is of course a discretization error that should vanish in the limit $\Delta \to 0$. In Fig. 15, we therefore show the comparison of Fig. 13 again, but this time, for one coarser $N_r = 400$ and one finer $N_r = 1600$ radial discretization. We can see that the agreement between the different discretizations of the derivative

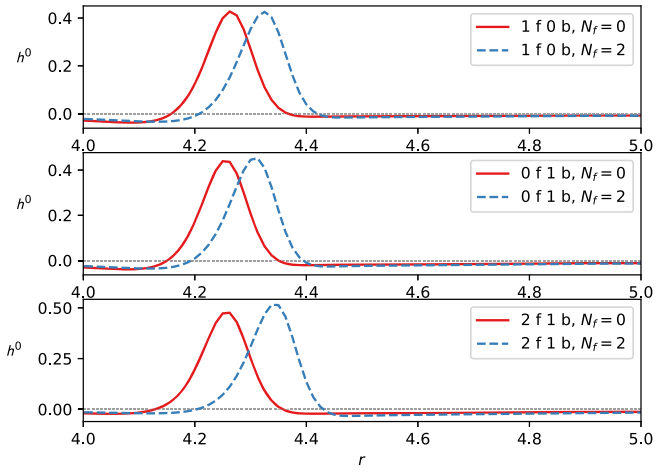

FIG. 14. Comparison of the vacuum contribution to the Hamiltonian density $\mathfrak{h}^0$ between the classical and semiclassical cases for three different discretizations of the derivative operator. Note that the important qualitative features, i.e., the different peak positions for the classical and semiclassical cases and the enhancement of $\mathfrak{h}$ by vacuum contributions in the peak region, are clearly present for all choices of the discretization.

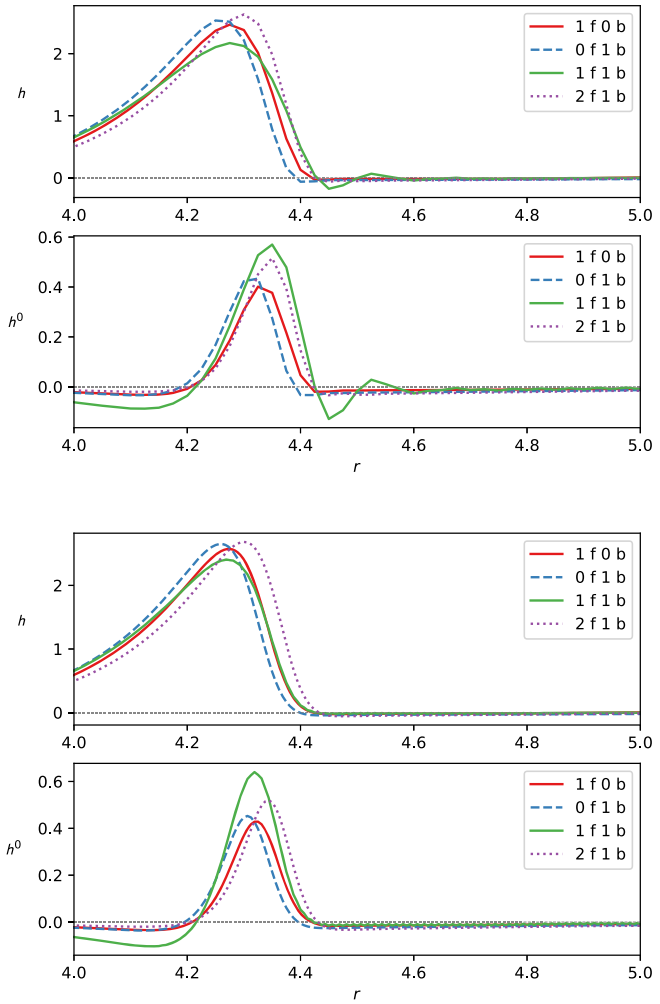

FIG. 15. Same as Fig. 13 for two different radial discretizations corresponding to $N_r = 400$ (top) and $N_r = 1600$ (bottom).

operator is slightly better for the finer radial discretization. Nonetheless, a more detailed study of this topic on substantially finer radial discretizations would be highly desirable.

E. Other variations of the update procedure

In addition to the radial discretization, we also have to check that the temporal discretization we use is fine enough. In Fig. 16, we compare results for three different time steps and find that they are virtually indistinguishable. For our finest radial discretization $N_r = 1600$, we actually observe some tiny discrepancies in the high frequency components around the position of the original peak, but even they are entirely negligible for the entire time evolution even beyond the safe zone.

Next, we would like to investigate the effect of classically absorbing boundary conditions as introduced in Sec. III E. In Fig. 17, we compare the time evolution between the two sets of boundary conditions and see that they agree rather precisely.

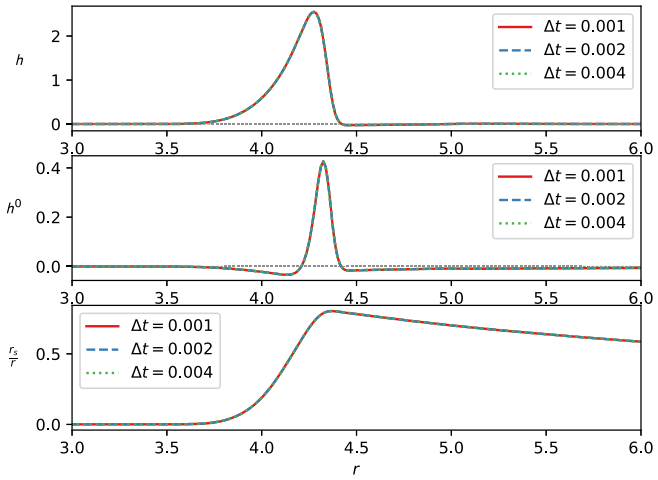

FIG. 16. Comparison of results for different time steps at $t = 12$.

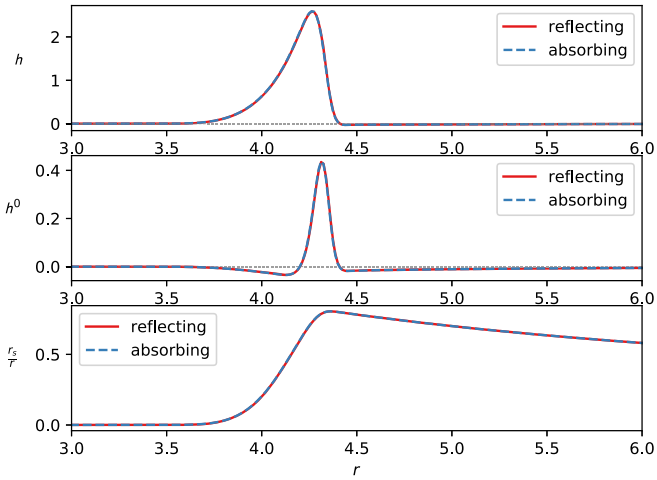

FIG. 18. The same plot as Fig. 17 but for a larger discretized volume $r_{N_r} = 12$.

The slight difference between the results with the two boundary conditions in Fig. 17 should of course be a finite volume effect. We can check this explicitly by performing the same comparison on a larger discretized volume with $r_{N_r} = 12$. We do this in Fig. 18 and indeed see that the difference between the two cases gets even smaller.

We can also study finite volume effects by comparing our default system with two systems that have a larger $r_{N_r} = 12$ and 14. As seen in Fig. 19, finite volume effects are very small.

In Fig. 20, we repeat this comparison for absorbing boundary conditions. We see that finite volume effects are even smaller in this case, indicating that the main contribution toward finite volume effects for our default system in fact comes from classical reflection off the outer boundary.

Next, we investigate varying the shape of the initial $\hat{\mathfrak{h}}$ of the scalar field from the usual Nuttall form (40) to the

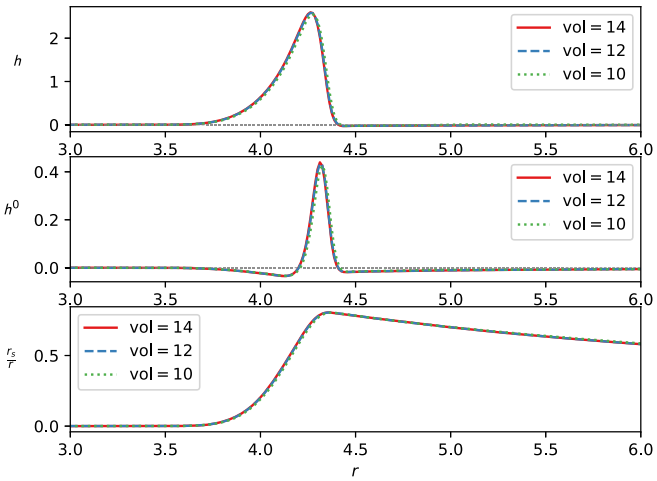

FIG. 19. Comparison of our default system of radial extent $r_{N_r} = 10$ at $t = 12$ with two systems of larger radial extent $r_{N_r} = 12, 14$ that are otherwise identical.

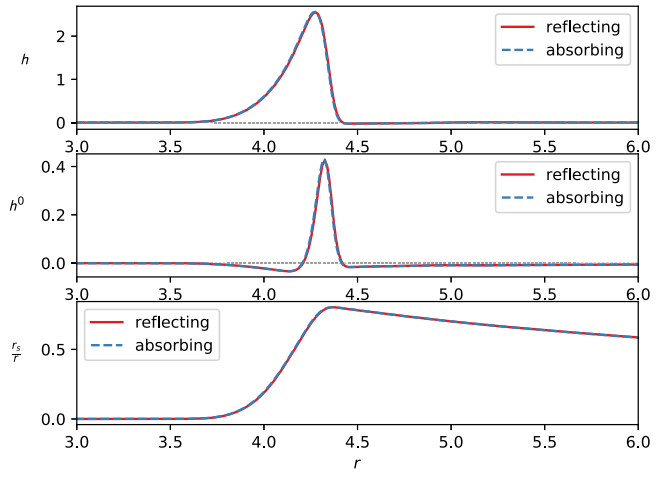

FIG. 17. Comparison of results with different boundary conditions at $t = 12$.

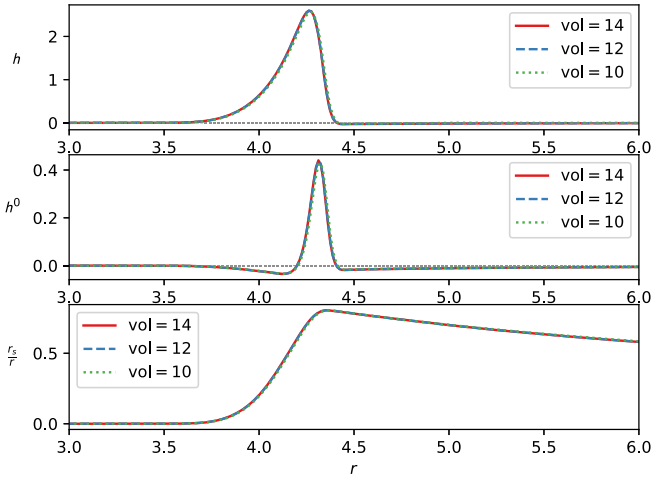

FIG. 20. The same as Fig. 19 but with absorbing boundary conditions.

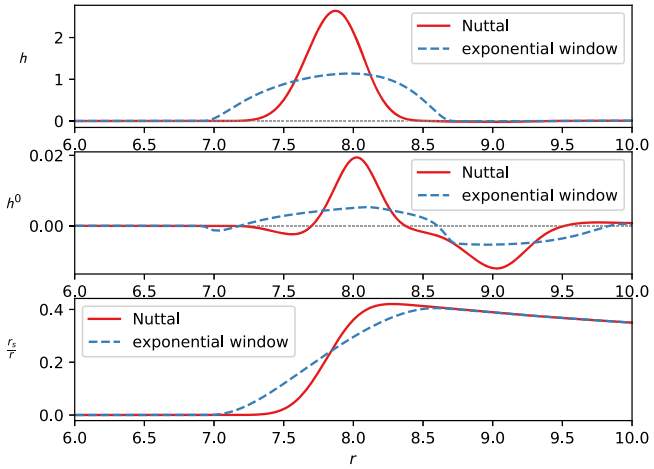

FIG. 21. Comparison of the semiclassical evolution with different initial scalar field bump shapes at $t = 2$.

exponential form (41). Figure 21 compares the two systems at an early time $t = 2$. Clearly, the exponential shape is less peaked than the Nuttall form, but the important qualitative feature, the enhancement of the Hamiltonian density $\mathfrak{h}$ around the peak region by the vacuum contribution $\mathfrak{h}^0$, is also prominent for the exponential bump.

At a later time $t = 12$, this property persists as is evident from Fig. 22. For the exponential bump, $\mathfrak{h}$ peaks at a larger radius, but the vacuum contribution $\mathfrak{h}^0$ does enhance the peak as it does for the Nuttall bump.

The next topic we would like to address is that of the error made by putting the scalar field at a rather small distance initially instead of asymptotically far away. We address this issue in a direct way by increasing the volume and putting the center of the initial bump to a larger distance and, more indirectly, by varying the vacuum subtraction. The effect of moving the initial scalar field farther outward on a larger system is displayed in Fig. 23. Since the shape of the bump changes as it propagates toward the center, we

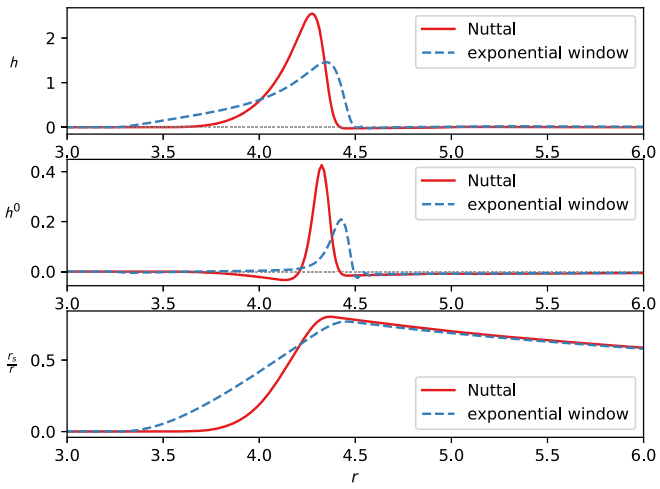

FIG. 22. The same as Fig. 21 but at a later time $t = 12$.

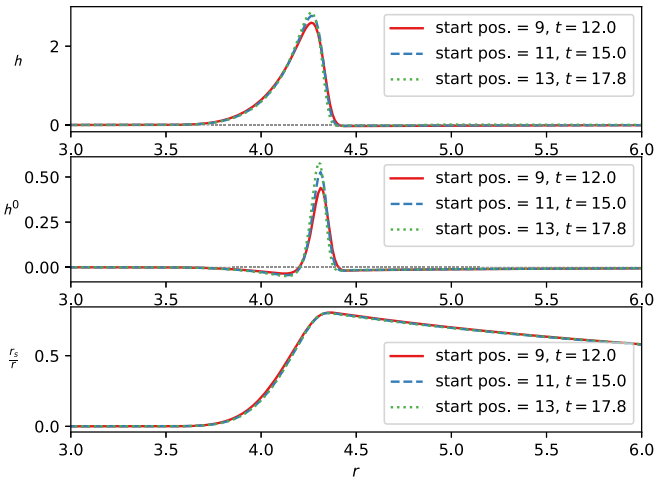

FIG. 23. Comparison of different starting positions of the scalar field. Results are compared at times where the respective systems have reached the same peak position of $\mathfrak{h}$ than the reference $t = 12$ for our default system. Fields that started farther out show a more pronounced peak of both $\mathfrak{h}$ and its vacuum contribution $\mathfrak{h}^0$.

do not expect the result from the different starting positions to agree exactly at the respective times when they have reached the same radial coordinate. Nonetheless, we can see that the differences are minimal with the bumps that started from a larger distance showing higher peaks.

The effect of changing the vacuum subtraction from the standard initial state normal ordering (21) to the free field subtraction (22) modified as described around (36) at an early time $t = 2$ is shown in Fig. 24.

Although we can see a marked difference in the vacuum contribution to the Hamiltonian density $\mathfrak{h}^0$ around the initial position of the scalar field, the effect on $\mathfrak{h}$ and even on $\mathfrak{h}^0$ outside this region is negligible. The difference

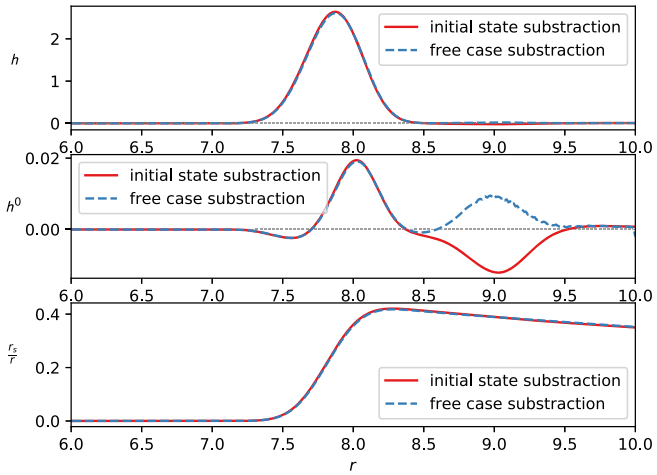

FIG. 24. Comparison of two vacuum subtraction procedures at time $t = 2$. The pronounced difference in $\mathfrak{h}^0$ between the two procedures is confined to the region of the initial bump position.

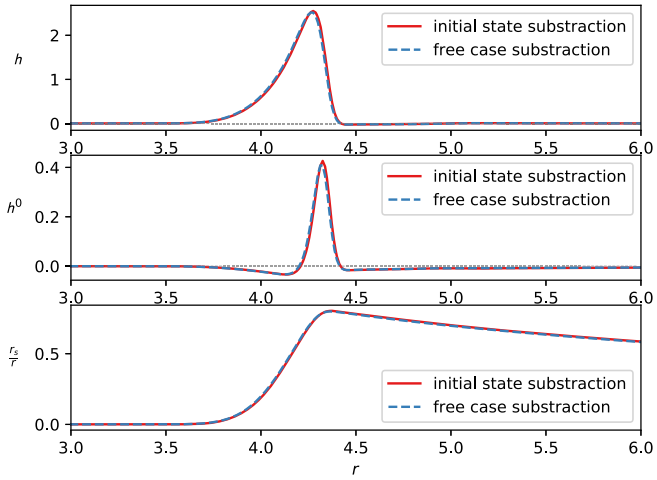

FIG. 25. The same as Fig. 24 but at a later time $t = 12$.

between the two procedures stays small also at later times, as seen in Fig. 25 for $t = 12$.

Finally, we would like to investigate the effect of changing the radial integration scheme from the standard δ-shell case (33) to the piecewise constant (34). As can be seen in Fig. 26, also this effect is entirely negligible at $t = 12$.

F. The operators q^0 and $\bar{q}$

It is quite instructive to investigate a bit the singular mode structure of the operators q^0 (20) and $\bar{q}$ (24). We start with the singular vectors $U_{\cdot k}$ and $V_{\cdot k}$ of q^0, which are interesting because they form the basis of the mode expansion. We plot a sample of the $V_{\cdot k}$ in Fig. 27. It is interesting that the shape of the initial bump is reflected in the modes with largest ω since they have support almost entirely in that region.

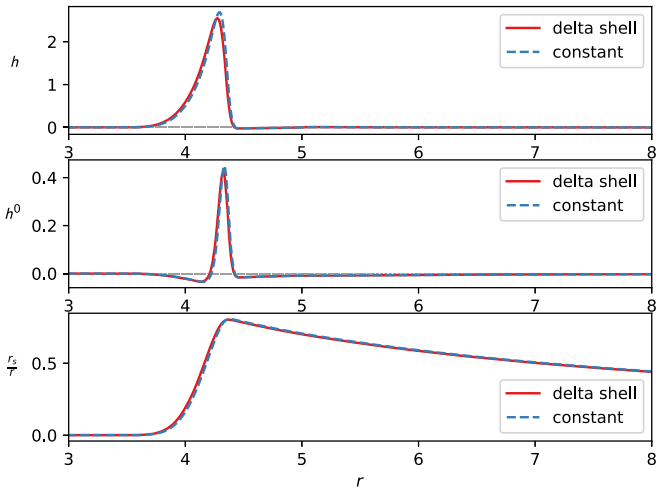

FIG. 26. Comparison of the time evolution with our two radial integration schemes at $t = 12$.

Turning to the operator $\bar{q}$ that is used in the time evolution of the scalar field, we are first interested in how its singular values change during the course of the evolution of the system. This is plotted in Fig. 28 for a representative selection of modes.

We see that during the course of the time evolution, the number of low modes increases while the high modes are thinned out. Deep within the unsafe region, we can even see a number of modes that reach singular values very close to $\omega = 0$ in a very short time. It is reasonable to assume that this concentration of low modes is connected to the onset of horizon formation. The closer the system gets to forming a real horizon, the more we expect modes to separate into those that are largely outside the forming horizon and take part in the usual time evolution and those modes that are largely inside and freeze as seen in coordinate time t (which is the physical time of an asymptotic observer). In order check whether this picture is correct, we define the "inside" and "outside" components of the singular vectors belonging to the singular value $\bar{\omega}_k$ as

$$(f_V^{\text{in}})_k^2 = \sum_{i=1}^{s} |\bar{V}_{sk}|^2 \qquad (f_V^{\text{out}})_k^2 = \sum_{i=s+1}^{N_r} |\bar{V}_{sk}|^2$$

$$(f_U^{\text{in}})_k^2 = \sum_{i=1}^{s} |\bar{U}_{sk}|^2 \qquad (f_u^{\text{out}})_k^2 = \sum_{i=s+1}^{N_r} |\bar{U}_{sk}|^2,$$

where we define s to be the index of the radial coordinate with the minimum d_i/r_i, i.e., the coordinate at which the system is closest to forming a horizon. Since the singular vectors are unit normalized, we have $(f_V^{\text{in}})_k^2 + (f_V^{\text{out}})_k^2 = (f_U^{\text{in}})_k^2 + (f_U^{\text{out}})_k^2 = 1$.

In Fig. 29, we plot the $f_{U/V}^{\text{in/out}}$ of a representative sample of modes. We see that with the exception of the few modes with the very highest ω, all modes start out with a substantial "in" component, which is of course what we expect from Fig. 27. As the bump and therefore the boundary between "in" and "out" moves toward the center, we first see the bulk of the modes gaining a substantial "out" component. At around $t = 10$, however, we see that the "out" components of the low modes start to decrease again while more and more of the higher modes cross over to be fully in the "out" region. Finally, deep in the unsafe region and at the point where Fig. 28 showed the appearance of modes with almost vanishing singular values, we see a sudden drop of the "out" components of these modes to almost zero, indicating that indeed they are frozen behind the developing horizon.

In order to display the relevant properties of the eigenmodes more compactly, we define the mode separation parameter,

$$s^2 = \frac{1}{2}(\langle (f_U^{\text{in}})_k^2 + (f_V^{\text{in}})_k^2 \rangle_{\text{in}} - \langle (f_U^{\text{in}})_k^2 + (f_V^{\text{in}})_k^2 \rangle_{\text{out}}), \tag{45}$$

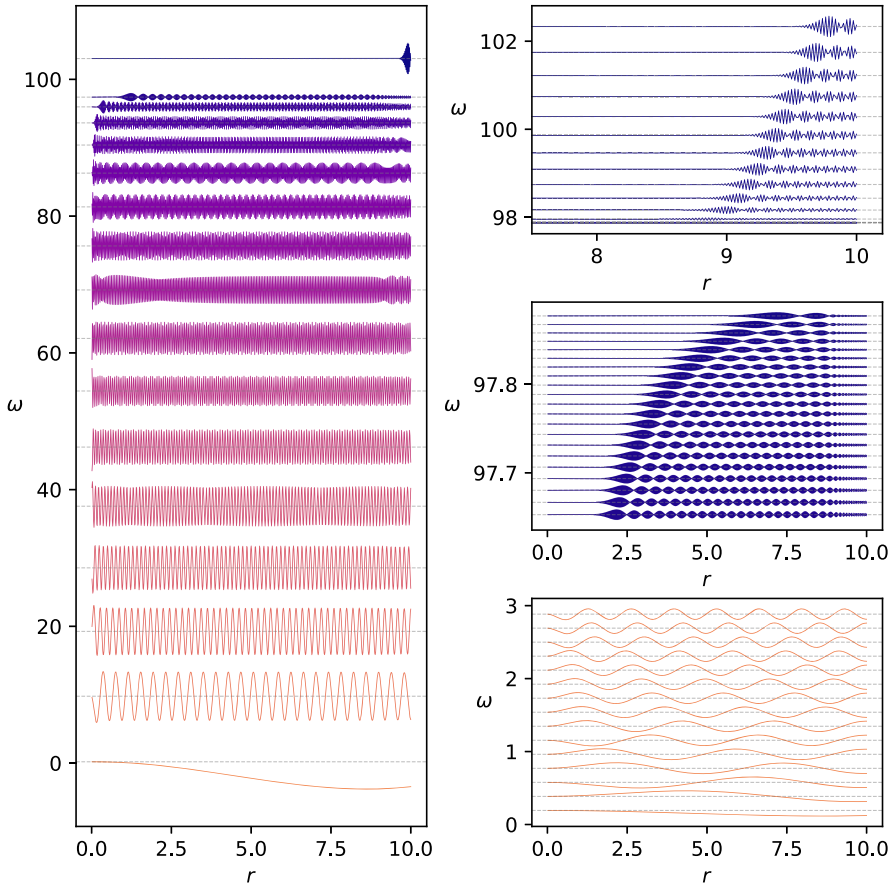

FIG. 27. Some of the singular vectors $U_{\cdot k}$ of the operator q^0 for our default system and their singular values ω_k. On the left-hand side, we plot every 50th mode starting from the mode with the lowest singular value and the mode with the highest singular value. On the right-hand side, we zoom in on three interesting regions for which we plot every mode. Note that the spacing of the modes decreases for increasing ω except for the few modes with the highest ω that are concentrated in the region of the original bump position.

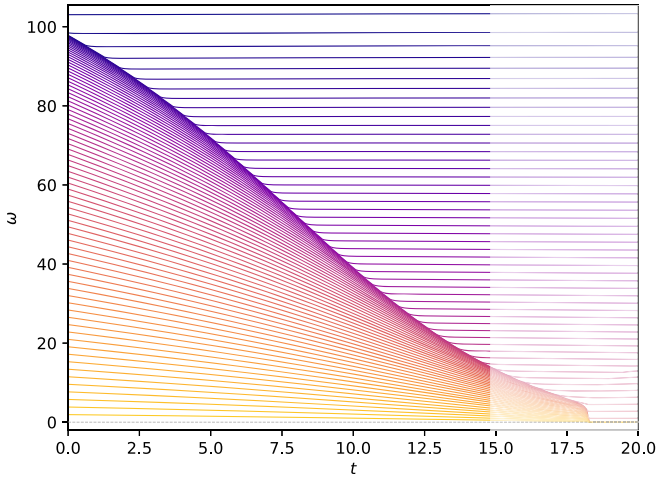

FIG. 28. Time evolution of the singular values $\bar{\omega}$ of $\bar{q}$. Starting from the highest, we plot every 10th $\bar{\omega}$. The shaded area on the right marks the unsafe region $t > t_{\text{safe}}$.

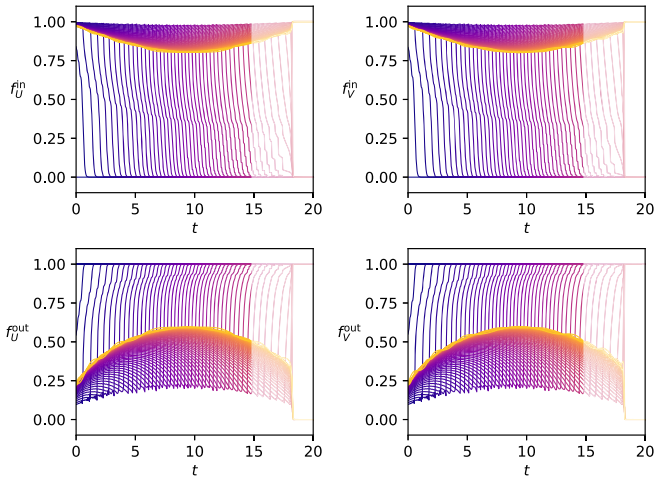

FIG. 29. The "inside" and "outside" components of the singular vectors of $\bar{q}$. We plot the same representative sample of motes as in Fig. 28 with the same color coding.

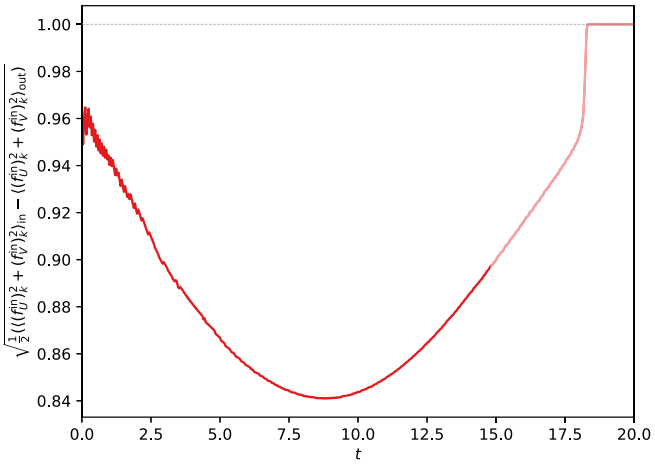

FIG. 30. The mode separation parameter s (45) versus t.

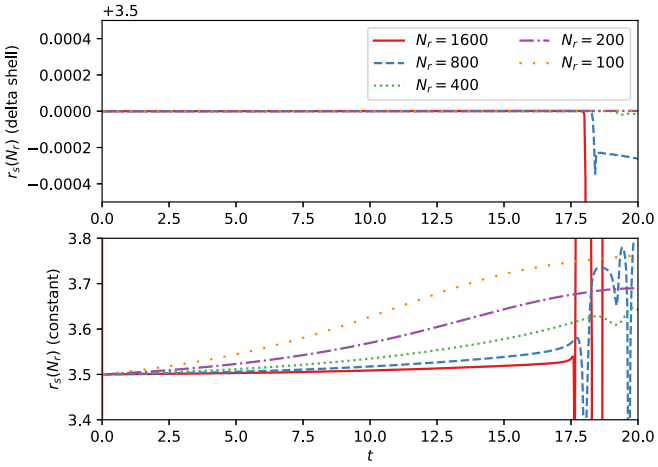

FIG. 31. Cross-check of how constant the effective Schwarzschild radius $r_s = r_{N_r} - d_{N_r}$ is on the outermost shell.

where $\langle\cdot\rangle_{\text{in}}$ denotes the average over all "inside" modes, which we arbitrarily define as those modes with $(f_U^{\text{in}})_k + (f_V^{\text{in}})_k > 1$. Correspondingly, $\langle\cdot\rangle_{\text{out}}$ denotes the average over all "outside" modes, which are those that do not fulfill this condition. When a horizon forms, we expect the modes to divide into those that have support exclusively inside the horizon and those that have support exclusively outside. Thus, $s = 1$ indicates horizon formation.

In Fig. 30, we plot the mode separation parameter versus t. The horizon formation is clearly visible in the unsafe zone.

G. Consistency check

In the continuum, the last equation in (29), i.e.,

$$\dot{d} = -2\hat{\alpha} d \hat{\mathfrak{p}}_r,$$

together with the first one,

$$\frac{1-d'}{d} = \frac{\hat{\alpha}'}{\hat{\alpha}},$$

guarantees that when $\hat{\mathfrak{p}}_r$ vanishes in some finite region, the metric does not change there. Looking at our finite, discretized system as an approximation to the infinite continuum case, we of course have $\hat{\mathfrak{p}}_r = 0$ in the region $r > r_{N_r}$, i.e., outside of our outermost discrete coordinate. Consequently, if we had a perfect update algorithm, the metric parameters in the outside region, and thus, also d_{N_r} would never change.[7] Since this property follows from the one equation of motion that we never use explicitly, it is a useful cross-check of the validity and accuracy of our numerical implementation.

[7]Remember that $\hat{\alpha}_{N_r} = 1$ is fixed by our boundary condition for radial integration.

In Fig. 31, we plot $r_s = r_{N_r} - d_{N_r}$ throughout the semiclassical time evolution, varying the radial discretization and the radial integration scheme. We see that r_s is conserved to a relatively high accuracy with the δ-shell integration faring markedly better than the piecewise constant. We can also see that for the finer discretizations, the agreement breaks down at large t outside the safe region. This coincides with the explosion of the maximum h_i and the sudden separation of the eigenmodes that we had observed above.

H. Prospects of observing Hawking radiation

An obvious question at this point is whether there is any prospect, in our formalism, to observe the effects of Hawking radiation. Since we have no method at present to represent the state of the scalar field in the outgoing Fock space, the individual field quanta are of course inaccessible. We could, however, hope to see the related outgoing energy flux. We can do a quick order of magnitude estimate of an expected flux based on a potential horizon formation at r_s based on the Stefan-Boltzmann law. This estimate tells us to expect an energy flux of the order,

$$\mathfrak{h}_{,t} \sim \frac{N_c}{3840\pi r_s^2},$$

and a corresponding flux in $\mathfrak{p}$ according to (30). Plugging in our $r_s \sim 3$, we find that in our current setup, this is several orders of magnitude smaller than the peak value of even the vacuum part $\mathfrak{h}_f^0$ alone and poses a formidable challenge for future studies.

I. Computational aspects

All numerical results presented in this paper have been obtained with a standard Fortran 2008 code on a small number of standard PCs. A fully independent Julia code

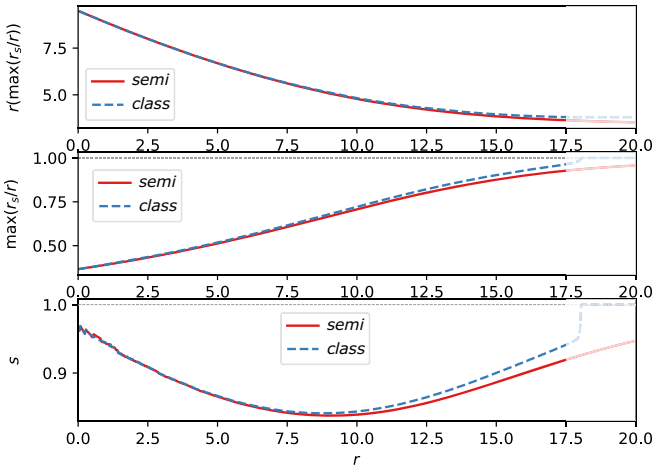

FIG. 32. Summary of the collapse for our default case with the finest radial discretization $N_r = 1600$. The top panel shows the Position of the maximum of r_s/r versus t where r_s is the local effective Schwarzschild radius of the metric. The middle panels shows the corresponding maximum value of r_s/r and the bottom panel shows the mode separation parameter s (45). The shaded region for large t corresponds to $t > t_{\text{safe}}$. We can clearly see that quantum effects enhance the potential horizon formation and move it radially outward. We also see that in the semiclassical case, our algorithm ultimately produces a horizon, which however happens in the region that we deem to be dominated by discretization artifacts.

was also written to cross check the main results. The most time consuming part of the algorithm is of course the SVD, especially in the implicit update step where it has to be invoked repeatedly. We have used standard LAPACK routines in double precision for this task and not exploited the fact that consecutive SVDs are of very similar matrices. We also have not used any form of optimization or parallelization of our code beyond standard compiler flags. Keeping this in mind, the time evolution of our default case scenario to $t = 20$ took about six hours of computer time on a single core of a standard PC. Although the SVD scales with the third power of the system size and Δt probably will have to be reduced for finer discretization, it should be possible to simulate substantially larger systems on parallel supercomputers.

V. CONCLUSIONS AND OUTLOOK

In this paper, we have presented a formalism to compute numerically the semiclassical gravitational collapse of a scalar quantum field in an initial coherent state in the angular momentum $l = 0$ approximation. Figure 32 summarizes our main result, which is the enhancement and radial outward shift of the peak of the energy density by quantum effects.

As a next step, we would like to investigate how the vacuum modes of the scalar field at higher angular momentum, which we have ignored in this first study, will change the behavior of the system. The formalism we have presented here can be generalized to take these modes into account [30], and a detailed numerical study is planned for a forthcoming publication.

On a more technical note, it would be nice to explore the possibility of inhomogeneous discretizations that would increase the radial resolution in the relevant region without too much computational overhead. In addition and possibly related is the question of finding a bump function that is optimized to have minimal overlap with the singular vectors of high ω on the specific metric.

Another direction we would like to explore in the future is the use of a different metric parametrization, e.g., with radially infalling coordinates. An even more ambitious goal would be to span the state of the scalar field in the Fock space basis of the final time, which would give us access to the outgoing particle content.

However, the ultimate question is whether the time evolution of the semiclassical collapse is unitary and if so, whether our formalism could in principle trace it from the initial infall through the (almost) formation of a horizon to the eventual evaporation via Hawking radiation in a situation where the corresponding classical theory does produce a horizon. Needless to say that the technical obstacles are huge.

Finally, a problem that we have completely ignored until now is whether semiclassical gravity is even applicable in the regime we are working in (the effective Schwarzschild radius of our entire system viewed from the outside is only ~3.5 Planck lengths). One direction for future investigations would therefore be to study larger systems with a higher scalar field content so that we are further in the semiclassical regime and check if our physical conclusions hold there, too.

ACKNOWLEDGMENTS

C. H. would like to thank Stephan Dürr for helpful discussions on the numerical aspects of this work. This work was in part supported by the DFG Grant No. SFB-TR 55 and by the Excellence Initiative of Aix-Marseille University-A*MIDEX (ANR-11-IDEX-0001-02), a French "Investissements d'Avenir" program, through the Chaire d'Excellence program.

[1] S. Hawking, Particle creation by black holes, Commun. Math. Phys. **43**, 199 (1975); Erratum, Commun. Math. Phys. **46**, 206 (1976).

[2] W. G. Unruh, Notes on black hole evaporation, Phys. Rev. D **14**, 870 (1976).

[3] T. Jacobson, Thermodynamics of Space-Time: The Einstein Equation of State, Phys. Rev. Lett. **75**, 1260 (1995).

[4] G. 't Hooft, On the quantum structure of a black hole, Nucl. Phys. **B256**, 727 (1985).

[5] A. Almheiri, D. Marolf, J. Polchinski, and J. Sully, Black holes: Complementarity or firewalls?, J. High Energy Phys. 02 (2013) 062.

[6] G. 't Hooft, Black hole unitarity and antipodal entanglement, Found. Phys. **46**, 1185 (2016).

[7] T. Jacobson, Introduction to quantum fields in curved spacetime and the Hawking effect, in Lectures on quantum gravity, *Proceedings, School of Quantum Gravity, Valdivia, Chile, 2002* (2003), pp. 39–89, arXiv:gr-qc/0308048.

[8] S. D. Mathur, The information paradox: a pedagogical introduction, Classical Quantum Gravity **26**, 224001 (2009).

[9] M. W. Choptuik, Universality and Scaling in Gravitational Collapse of a Massless Scalar Field, Phys. Rev. Lett. **70**, 9 (1993).

[10] D. Christodoulou, The problem of a selfgravitating scalar field, Commun. Math. Phys. **105**, 337 (1986).

[11] D. Christodoulou, Global existence of generalized solutions of the spherically symmetric Einstein scalar equations in the large, Commun. Math. Phys. **106**, 587 (1986).

[12] D. Christodoulou, The structure and uniqueness of generalized solutions of the spherically symmetric Einstein scalar equations, Commun. Math. Phys. **109**, 591 (1987).

[13] D. Christodoulou, A mathematical theory of gravitational collapse, Commun. Math. Phys. **109**, 613 (1987).

[14] D. S. Goldwirth and T. Piran, Gravitational collapse of massless scalar field and cosmic censorship, Phys. Rev. D **36**, 3575 (1987).

[15] M. D. Roberts, Scalar field counterexamples to the cosmic censorship hypothesis, Gen. Relativ. Gravit. **21**, 907 (1989).

[16] P. R. Brady, Analytic example of critical behavior in scalar field collapse, Classical Quantum Gravity **11**, 1255 (1994).

[17] Y. Oshiro, K. Nakamura, and A. Tomimatsu, Critical behavior of black hole formation in a scalar wave collapse, Prog. Theor. Phys. **91**, 1265 (1994).

[18] A. V. Frolov, Selfsimilar collapse of scalar field in higher dimensions, Classical Quantum Gravity **16**, 407 (1999).

[19] M. Purrer, S. Husa, and P. C. Aichelburg, News from critical collapse: Bondi mass, tails and quasinormal modes, Phys. Rev. D **71**, 104005 (2005).

[20] C. Gundlach and J. M. Martin-Garcia, Critical phenomena in gravitational collapse, Living Rev. Relativity **10**, 5 (2007).

[21] B. Berczi, P. M. Saffin, and S.-Y. Zhou, Gravitational collapse with quantum fields, Phys. Rev. D **104**, L041703 (2021).

[22] B. Berczi, P. M. Saffin, and S.-Y. Zhou, Gravitational collapse of quantum fields and Choptuik scaling, J. High Energy Phys. 02 (2022) 183.

[23] A. Tomimatsu, Quantum gravitational collapse of a scalar field and the wave function of black hole decay, Phys. Rev. D **52**, 4540 (1995).

[24] D. Bak, S. P. Kim, S. K. Kim, K.-S. Soh, and J. H. Yee, Wave functions for quantum black hole formation in scalar field collapse, Phys. Rev. D **61**, 044005 (2000).

[25] D. Bak, S. P. Kim, S. K. Kim, K.-S. Soh, and J. H. Yee, Black hole decay and quantum instantons, Phys. Rev. D **62**, 047504 (2000).

[26] T. Vachaspati and G. Zahariade, Classical-quantum correspondence and Hawking radiation, J. Cosmol. Astropart. Phys. 04 (2019) 013.

[27] H. Kawai and Y. Yokokura, Black hole as a quantum field configuration, Universe **6**, 77 (2020).

[28] D. N. Page, Particle emission rates from a black hole: Massless particles from an uncharged, nonrotating hole, Phys. Rev. D **13**, 198 (1976).

[29] C. G. Callan, Jr., S. B. Giddings, J. A. Harvey, and A. Strominger, Evanescent black holes, Phys. Rev. D **45**, R1005 (1992).

[30] J. N. Guenther, C. Hoelbling, and L. Varnhorst, Real time dynamics of a semiclassical gravitational collapse of a scalar quantum field, Proc. Sci., LATTICE2021 (**2021**) 156 [arXiv:2111.15562].

[31] N. Bogolyubov, On a new method in the theory of superconductivity, Nuovo Cimento **7**, 794 (1958).

[32] A. Nuttall, Some windows with very good sidelobe behavior, IEEE Trans. Acoust. Speech Signal Process. **29**, 84 (1981).